Carbon 202 (2023) 528–546

Contents lists available at ScienceDirect

Carbon

journal homepage: www.elsevier.com/locate/carbon

Atomistic modeling of tensile deformation and fracture of carbon fibers: Nanoscale stress redistribution, effect of local structural characteristics and nanovoids

Miao He [a,b], Mikhail I. Arefev [a], Kaushik Joshi [a], Leonid V. Zhigilei [a,*]

[a] Department of Materials Science and Engineering, University of Virginia, 395 McCormick Road, Charlottesville, VA, 22904-4745, United States
[b] Department of Mechanical Engineering, University of Michigan, Ann Arbor, MI, 48109, United States

A B S T R A C T

The mechanisms of tensile deformation and fracture of carbon fibers are investigated in large-scale molecular dynamics simulations. The simulations performed for computational samples with different structural characteristics enable analysis of the structural sensitivity of the mechanical properties. It is found that the carbon fiber nanostructure can be represented by a fine (nanoscale) mixture of stiff and soft regions. Despite the nanoscale structural heterogeneity of the computational fibers, their fracture strain and tensile strength exceed the experimental values by almost an order of magnitude. This observation is explained by the ability of the carbon fiber nanostructure, largely consisting of curved and folded layers of turbostratic carbon, to exhibit continuous nanoscale load redistribution during the deformation. The transient, fluid nature of a percolating cluster of stress-holding structural elements prevents stress localization at the early stage of the deformation and enables the fiber nanostructure to adapt to the increasing load. Overall, the results of the simulations suggest that the design of advanced carbon fiber manufacturing and post-processing methods focused on the elimination of critical mesoscopic structural defects (internal voids, foreign inclusions, and surface flaws) can yield a substantial increase in the strength and fracture strain of carbon fibers.

1. Introduction

Carbon fiber (CF) is a lightweight, ultra-strong material widely used in aerospace, automotive, defense, sports equipment, and wind energy sectors [1,2]. The increasing demand for CFs, largely driven by the quest for energy efficiency in transportation and the rapid growth of wind energy industry, are stimulating the exploration of a broader range of molecular precursors [1,3–5], structure-templating agents [6–8], and CF manufacturing procedures [9–11] aimed at producing high-performance fibers at a reduced cost. This exploration is guided by investigations focused on revealing the relationships between CF microstructure and properties [9,12–15].

The microstructure of CFs has a complex hierarchical character, with both the nanostructure and mesoscopic structural organization defined by the choice of molecular precursors and CF manufacturing conditions. At the nanoscale, the relative fractions of turbostratic, graphitic, and amorphous regions, the size of the graphitic and turbostratic domains, and the degree of alignment of carbon layers along the fiber axis are among the key factors affecting the mechanical properties of CFs. The formation of large, well-ordered graphitic crystallites is usually observed in mesophase pitch CFs, while the turbostratic structure featuring wrinkled, folded, and crosslinked layers of carbon is the main structural constituent in most of the CFs produced from other precursors, such as polyacrylonitrile (PAN) [1,9,12]. The high degree of crystalline ordering in mesophase-pitch-based CFs leads to the large Young's modulus approaching the theoretical value for graphene, ~1 TPa, but also reduces the tensile strength and fracture strain [12]. The record values of the tensile strength, up to 13 GPa, measured with short effective gauge length [16,17] for PAN-based CFs, on the other hand, are attributed to the highly homogeneous, axially aligned turbostratic nanostructure revealed in high resolution transmission electron microscopy (HRTEM) imaging and X-ray diffraction analysis of the CFs [12,16].

The high fraction of sp^3 hybridized carbon atoms, reflecting the presence of amorphous regions and crosslinks between the graphitic/turbostratic carbon layers, is usually associated with large compressive [4] and shear moduli [18,19], but has a negative effect on the tensile strength. The less crosslinked structures, on the other hand, can undergo a higher degree of structural alignment in the course of polymer fiber stretching and high-temperature carbonization, thus yielding CFs with crystallites well aligned along the fiber axis. The increased alignment and large size of graphitic crystallites is generally associated with enhanced tensile strength and modulus [12,13]. The alignment of structural elements of the CF nanostructure can be facilitated by the

* Corresponding author.
E-mail address: lz2n@virginia.edu (L.V. Zhigilei).

https://doi.org/10.1016/j.carbon.2022.10.092
Received 2 September 2022; Received in revised form 27 October 2022; Accepted 31 October 2022
Available online 3 November 2022

addition of structure-templating agents, such as carbon nanotubes [6], graphene [7], and graphene oxide [8]. The templating elements promote the molecular alignment in precursor polymer fibers [7] and serve as nucleating agents [20] that facilitate the formation of larger crystalline regions aligned along the CF axis at the carbonization and graphitization stages of CF manufacturing. These structural changes are found to produce a substantial increase in the tensile strength and Young's modulus of PAN-based CFs [6–8].

The overgrowth of the graphitic crystallites, however, may also produce larger pores and higher stress concentration, thus negatively affecting the tensile strength [1,12]. In particular, the nonmonotonous dependence of the tensile strength on the graphitization temperature observed in the manufacturing of PAN-derived CFs, which exhibits a maximum at about 1500 °C and decrease at higher temperatures [14,21], can be correlated with the accelerated increase in the size of the graphitic domains with increasing graphitization temperature [22]. This correlation is supported by the results of recent atomistic simulations, where the tensile strength and fracture strain are observed to decrease with increase in the graphite content in CF structures featuring large fractions of the graphitic constituent [23].

In addition to the nanoscale structure, the mechanical properties of CFs are strongly affected by the mesoscopic morphology/texture that is highly sensitive to the choice of molecular precursor and conditions of fiber manufacturing. The fiber cross-sections can exhibit random/homogeneous, radial, circular (onion skin or tree-ring like), or core-skin morphology [1–3,9,10,13–16,19], which defines the types of defects and stress concentrators present in the fibers. It has been found, in particular, that CFs with core-skin structure featuring multi-layer graphitic crystallites in the outer layer of the fiber have higher Young's modulus but lower tensile strength as compared to fibers with homogeneous cross-sectional structure [24–26]. The deleterious effect of the skin layer on the tensile strength of CFs is commonly attributed to the mismatch in the elastic properties between the softer core and stiffer skin layer [25,27], leading to the heterogeneous stress distribution during deformation [25] and generation of microcracks in the course of CF manufacturing [24,27]. The results of recent computational study [28], however, suggests that the formation of a high-quality skin layer may suppress the crack nucleation at the core-skin interface and produce a simultaneous increase in the Young's modulus and tensile strength of the CFs.

In general, the tensile strength of the strongest currently manufactured CFs is still largely limited by the presence of microvoids, foreign inclusions, surface microcracks, and other stress-raising defects [12–16,29,30], rather than the intrinsic fiber nanostructure. This is apparent from the significant increase in the tensile strength with decreasing gauge length reported for PAN-based CFs [16], as well as the superior mechanical properties of carbon nanofibers with diameters reduced to hundreds of nanometers [31–33]. Both observations can be attributed to the decreasing probability of finding large structural defects in the microstructure of smaller test samples.

The complex hierarchical micro/nanostructure of carbon fibers presents a significant challenge for the theoretical description and continuum-level modeling of CF mechanical properties. Despite the continuous accumulation of experimental data on the dependence of the CF strength and stiffness on the degree of crystallinity, orientational anisotropy, relative fractions of sp^2 and sp^3 hybridized carbon, porosity, presence of various defects, and mesoscopic structural morphology of the fiber, the micromechanical models of the elastic behavior and fracture of CFs still rely on highly simplified representations of the structural constituents and qualitative description of their collective response to mechanical loading, *e.g.*, Refs. [1,9,13,18,19,25,28,34,35].

Molecular dynamics (MD) computer simulations have a potential for revealing the atomic-scale structural characteristics and processes that control the mechanical behavior and properties of CFs. The detailed atomistic information obtained in MD simulations can enable the design of advanced micromechanical models fully accounting for the complexity of the CF microstructure and provide guidance for tailoring the microstructure through the choice of molecular precursors and manufacturing conditions. Indeed, the MD simulations have been used for the exploration of chemical reactions and nanoscale structural transformations occurring at different stages of CF manufacturing, including the effect of the structure-templating agents (graphene and carbon nanotubes) [7,36], carbonization temperature [11], pressure [37], and type of the molecular precursor [4,38–41].

The investigation of the mechanical behavior and properties, however, has been hindered by the relatively small scale of computational systems accessible for reactive MD simulations. The small atomic systems representing local structures of CFs can still be used for calculation of the elastic moduli [4,42] and investigation of the mechanical response of structural features defining the strength of CFs, such as nanovoids intrinsic to the highly distorted turbostratic constituent of CFs [43], topological defects in graphene sheets [44], misoriented stacking of graphitic domains [45], and graphitic-amorphous interfaces [45]. Larger computational samples required for analysis of the stress-strain relationship and fracture have been constructed from small cuboid blocks of graphite [46] or distorted graphitic sheets perfectly aligned along the axis of the fiber [47]. Recent development of a computational approach for the generation of fully three-dimensional (3D) CF structures consisting of turbostratic, graphitic, and amorphous constituents [23] has enabled the initial exploration of the mechanical deformation and fracture of realistic computational CF structures [11,23]. The dimensions of the computational systems used in these initial studies, ~20 nm along the fiber axis and ~6–7 nm in the directions perpendicular to the fiber axis, however, are comparable to (only 2–3 times larger than) the sizes of the largest structural features, such as graphitic crystallites and internal voids [23]. As a result, the analysis of the stress concentration and redistribution during the mechanical deformation can be affected by artifacts introduced by the periodic boundary conditions applied in the simulations.

In this paper, we use the general methodology developed in Ref. [23] to generate computational samples that are sufficiently large to provide a realistic representation of the collective behavior of multiple elements of the CF nanostructure in the course of mechanical deformation and fracture. The large-scale MD simulations are then used for investigation of the evolution of atomic-level stresses, nanoscale load transfer, and initiation of fracture during the tensile deformation of computational samples with different structural characteristics. The results of the simulations reveal the ability of intrinsic CF nanostructure consisting of a fine mixture of turbostratic, amorphous and graphitic regions to support stresses more than twice higher than the record values observed in experiments, thus suggesting that significant progress in making stronger fibers may be achieved through the elimination of mesoscopic structural heterogeneities and defects.

2. Computational methods for generation and characterization of model CFs

In this section, we first provide a description of the computational procedure used for the generation of four CF computational samples with distinct structural characteristics, then explain the choice of the interatomic potentials used in the sample preparation and mechanical testing of the computational CFs, and then describe the local (atomic level) and average (macroscopic) parameters applied for the structural characterization and analysis of the mechanical deformation of CFs. The focus of the structural characterization and evaluation of the mechanical properties is on the parameters that can be directly probed in experiments.

2.1. Generation of CF microstructure

The direct modeling of the complex chemical reactions and structural transformations involved in the multi-step CF manufacturing

process [1,9,12–14] are far beyond the capabilities of atomistic simulations. Therefore, the computational CF samples with nanostructure similar to that of real CFs are generated in the present study with a simple and computationally efficient method developed in Ref. [23]. In this method, the atomic configurations are produced through structural self-assembly and reactive fusion of idealized ladder structures consisting of three rows of hexagonal carbon rings saturated by hydrogen atoms along the edges. While similar hydrogenated and nitrogenated ladders have been identified in stabilized PAN fibers used in the CF manufacturing [1,2,12–14], the computational procedure is not aimed at reproducing the complex processes occurring during the carbonization and graphitization of polymer fibers under experimental conditions of carbon fiber manufacturing. Rather, the computational method is designed to provide flexibility for controlling the structural characteristics of model CF microstructures, such as the relative fractions of turbostratic, graphitic, and amorphous domains, the void size distribution, as well as the degree of orientational ordering. The details of the computational method used for the generation of CF microstructures are described in Ref. [23], and below we only provide the parameters adapted for the generation of large samples used in the present study.

As the first step in the generation of the CF microstructures, an initial configuration was built by packing individual (non-stacked) ladder structures of 5 different lengths. Each ladder consisted of three rows of hexagonal carbon rings with edges of the ladders saturated with hydrogen atoms. The total of 4800 2.3-nm-long ladders (27 carbon rings each), 4000 4.7-nm-long ladders (57 carbon rings each), 4000 7.1-nm-long ladders (87 carbon rings each), 2000 9.6-nm-long ladders (117 carbon rings each), and 1000 12.0-nm-long ladders (147 carbon rings each) were used in the generation of the initial sample. The ladders were packed into an orthogonal box with dimensions of 80 nm × 40 nm × 40 nm and were preferentially aligned along the fiber axis (*x*-axis), so that the initial orientation of a ladder's longest axis is within 10° with respect to the axis of the CF. The packing was performed with PACKMOL code [48], which produced a system with density of 0.46 g/cm^3. This initial system, shown in Fig. 1a, consists of 2,992,400 carbon and 850,800 hydrogen atoms. To obtain the final CF microstructures, the initial system undergoes an energy minimization procedure first, and is then subjected to the following sequence of constant-temperature and constant-pressure (NPT) MD simulations:

(1) The system is heated to 300 K and equilibrated at 300 K and a hydrostatic pressure of 1 atm;
(2) The system is heated to 900 K and compressed by applying hydrostatic pressure P_{step2};
(3) The hydrogen atoms attached to the armchair edges of the ladders are removed, the pressure is reduced to 1 atm in the axial direction (*x*-direction), and the system is annealed at 900 K;
(4) The remaining hydrogen atoms are removed from the zigzag edges of the ladders, the pressure is reduced to 1 atm in the transverse directions (*y*- and *z*-directions), and the system is annealed at 900 K;
(5) The system is heated from 900 K to 2000 K, annealed at 2000 K for 250 ps, and cooled back to 300 K.

All of the NPT MD simulations listed above are performed with periodic boundary conditions applied in all three directions and pressure control applied independently in each direction. In order to investigate the effect of the variation in the structural characteristics on mechanical properties, four different CF samples, denoted as CF1, CF2, CF3, and CF4, are prepared by varying the level of compression at step (2) and the rates of dehydrogenation at steps (3) and (4). The computational sample CF1 is compressed at $P_{step2} = 0.15$ GPa before the carbonization, while the other three samples are compressed at $P_{step2} = 0.3$ GPa. In the preparation of computational samples CF1 and CF2, all hydrogen atoms attached to the same type of sites along the edges of the ladders (armchair or zigzag) are removed simultaneously, while for the other two samples the dehydrogenation is done gradually, at a constant rate of 10 and 5 hydrogen atoms removed every 10 steps (the time step is 0.1 fs) for samples CF3 and CF4, respectively. The final CF microstructures have densities ranging from 1.69 to 1.78 g/cm^3, the length in the axial direction from 54.3 to 57.5 nm, and the dimensions perpendicular to the fiber axis from 23.9 to 25.9 nm, as can be seen from Table 1. The representative atomic structure shown in Fig. 1b and c for sample CF2 demonstrates that the procedure described above produces a fairly homogeneous nanostructure featuring curved and folded layers of turbostratic carbon, small elongated nanovoids, and small isolated islands of more ordered graphitic structure. While the quantitative structural analysis of the computational samples is provided in Section 3.1, we note that the densities of the CF microstructures are comparable to the typical experimental range of 1.7–2.0 g/cm^3 for high-strength PAN-based CFs [12,13,16,17,22,49] and the visual picture of the atomic configuration is consistent with the results of experimental characterization of PAN-based CF [1,9,12,15,16].

2.2. Interatomic potentials

The MD simulations contributing to the preparation of the CF microstructures are performed with the reactive bond-order AIREBO-M interatomic potential [50] implemented in the LAMMPS code [51]. This potential provides an adequate description of reactive dynamics in hydrocarbon systems but fails to describe the stress-strain dependence in the vicinity of tensile fracture strength. In particular, a sharp nonlinear increase in stress is observed in simulations of carbon nanotubes [52]

Table 1
Density and dimensions of four computational CF samples used in MD simulations of tensile deformation and fracture.

	Density (g/cm^3)	Dimensions (nm)
CF1	1.71	54.8 × 24.6 × 25.9
CF2	1.78	54.3 × 24.2 × 25.4
CF3	1.69	56.6 × 24.3 × 25.6
CF4	1.72	57.5 × 23.9 × 25.3

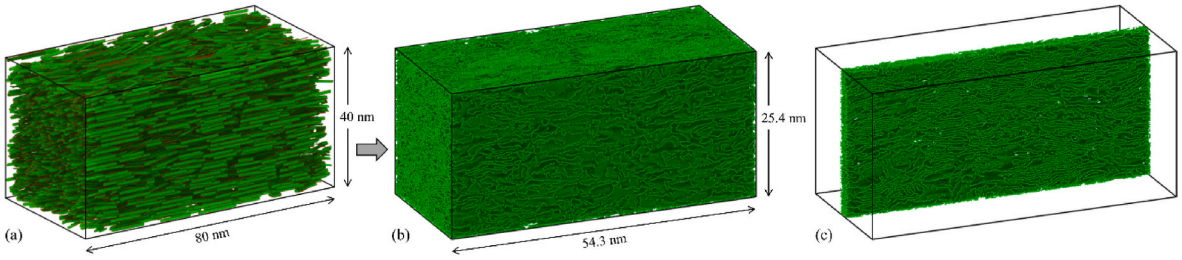

Fig. 1. Illustration of the preparation of CF microstructure: from the initial system of randomly stacked axially-aligned hydrogenated carbon ring ladders (a) to a compact CF2 nanostructure (b) through compression, thermal annealing and dehydrogenation. A longitudinal 2-nm-thin slice of the microstructure is shown in (c). The hydrogen atoms in (a) are shown by small red dots. (A colour version of this figure can be viewed online.)

and graphene [53] prior to fracture, leading to overestimations of fracture strain and strength. The artificial strain hardening at high tensile stresses is related to the steep cutoff function used in AIREBO potential for switching off the bonding interactions within a narrow range of distances between the first and second nearest neighbor shells [54,55], which produces an effective strengthening of C–C bonds near the inflection point of the potential. An *ad hoc* solution based on extending the cutoff distance while considering bonding interactions between the nearest neighbor atoms only [54] enables a more realistic representation of brittle fracture in diamond [54] and graphene [56,57]. This approach has also been used in the simulation of tensile deformation and fracture of CFs performed for a small computational system, about 7 nm × 7 nm in the directions perpendicular to the fiber axis [11,23]. The initial test simulations performed for a larger system used in the present study, however, reveal that the approach based on the modification of the switching function is not suitable for the description of a more complex fracture behavior involving both bond scission and formation of new bonds during the irreversible (plastic) deformation and fracture.

Therefore, the interatomic interactions in the simulations of tensile testing of the computational CF samples are described in this work by a more computationally expensive [58] ReaxFF potential [59,60] with a parameter set CHON-2019 developed in Ref. [39]. This parameterization is based on an earlier C-2013 parameter set for carbon-carbon interactions [61], which has been found to reproduce fairly well the experimental data and predictions of DFT calculations on the mechanical properties of diamond, graphite, carbon nanotubes, and amorphous carbon [62].

2.3. Structural characterization of computational CF structures

The structural characterization of the CF samples is performed with a toolset developed and applied to smaller CF samples in Ref. [23]. Briefly, the hybridization state of a carbon atom in an atomic configuration prepared with the AIREBO-M potential is identified by counting the number of nearest neighbor atoms located within a cutoff distance of 1.7 Å from the atom of interest. The sp, sp^2 and sp^3 hybridization states correspond to the atoms with two, three and four nearest neighbors, respectively. During the MD simulations of tensile deformation, the hybridization state of each carbon atom is evaluated by counting the number of neighbor atoms, which is given by the ReaxFF potential with a bond order cutoff of 0.3.

A combination of hybridization state of carbon atoms, their participation in the hexagonal graphene layers, and the energy of inter-layer interaction is used to distinguish between the turbostratic, graphitic, and amorphous regions in the CF nanostructure [23]. The dominant constituent in all computational samples is the turbostratic carbon [63] composed of bent and distorted graphene layers stacked together with a varying degree of misalignment. The carbon atoms that belong to graphitic regions are identified as atoms in the sp^2 hybridization state that have a potential energy that is within 30 meV/atom from the energy of a carbon atom in an ideal graphite crystal at 0 K (−7.45 eV/atom predicted by the AIREBO-M potential). The potential energy of each atom is calculated by cooling the system from 300 K to 1 K in an NPT MD simulation and then applying energy minimization to obtain a configuration at 0 K. The degree of graphitization in a CF sample is defined as the fraction of graphitic atoms with respect to the total number of atoms in the system.

The characteristic sizes of the ordered graphitic domains in the CF microstructures are also evaluated from one-dimensional diffraction profiles calculated for the computational samples using a histogram-based method described in Refs. [23,64]. The calculations are performed with a cutoff for interatomic distances of 12 nm, which is the largest possible cutoff for systems with lateral dimensions of about 24 nm (see Table 1). The spurious ripples introduced by the cutoff are suppressed by a damping function described in Ref. [64], and the histogram bin size used in the calculations is 0.02 Å. The thickness of ordered domains along the direction normal to the stacking of graphitic planes, L_c, as well as the average lateral extent of the ordered domains along the graphitic planes, L_a, is estimated using the Scherrer equation, $L = K/\Delta Q$, where $K = 5.78$ [65] and ΔQ is defined as the full width at half maximum (FWHM) of the Gaussian approximation of a diffraction peak produced by crystal planes normal to the direction in which the dimension L of the ordered domain is measured. The degree of the orientational ordering in the computational samples is characterized by two-dimensional (2D) diffraction patterns calculated using a histogram-based approach described in Ref. [66]. To mitigate a finite-size artifacts, we apply a damping function to reduce the termination effect and subtract a term accounting for the average atomic density, as described in Ref. [66]. The cutoff for interatomic distances in 2D calculations is decreased to 8 nm to improve computational efficiency without a significant loss of structural information. The 2D cross-sections of the reciprocal space are calculated in a polar coordinate system with an angular step of 0.25°.

A prominent feature of the CF structure that has direct implications on the mechanical properties is the presence of nanoscale pores or voids. To characterize the sizes and shapes of the pores, a 3D grid of cubic cells with a size of ~0.4 nm was superimposed on the atomistic configuration. A pore is defined as a cluster of two or more cells with less than two atoms in each cell. The centers of the cells are used to identify the pore faces, and the pore size is defined as a line that connects the farthest surfaces of the pore without crossing the pore boundary [23].

The degree of the orientational ordering in the CF samples is quantified through identification of carbon rings, followed by analysis of the orientation of carbon rings with respect to the axis of the fiber [23]. The carbon rings are defined as simple loops of nearest neighbor carbon atoms with no crossovers and with the maximum ring size of 9. The overall degree of orientational order in a CF sample is quantified by the Herman's Orientation Factor (HOF) calculated based on the orientation of all 5-, 6-, and 7-member rings in the computational sample. The values of HOF can range from −0.5 to 1.0, with HOF = −0.5 for perfect alignment of all rings along the fiber axis and HOF = 0 for random orientation of the rings. The orientational ordering of graphitic and turbostratic carbon planes with respect to the fiber axis is also reflected in the two-dimensional (2D) diffraction patterns calculated for the computational samples with a method described in Ref. [66].

The computer codes implementing the methods used in the structural characterization of the CF samples and the calculation of 2D diffraction patterns are available from Refs. [67,68].

2.4. Characterization of the mechanical behavior of CFs

The characterization of mechanical properties of the computational CF structures is done based on the results of tensile tests, where the four CF samples are stretched along the fiber axis (x-axis) with an engineering strain rate of 4×10^8 s^{-1}. Although this strain rate is much higher than those used in experimental studies, it has been demonstrated in the simulations of mechanical deformation of graphene, carbon nanotubes, and diamond that the effect of strain rate on the stress-strain dependences remains insignificant up to the strain rates as high as 22×10^8 s^{-1} [69]. The lack of strain rate dependence can be attributed to the high energy barriers for carbon bond scission and rearrangements in carbon materials, which can be hardly affected by thermal fluctuations at 300 K. The values of the normal stress components in the directions perpendicular to the axis of the fiber (y and z directions) are maintained at a constant level that corresponds to a pressure of 1 atm during the deformation. The parameters characterizing the mechanical behavior of the CF samples, such as the Young's modulus, tensile fracture strain and strength are evaluated directly from the stress-strain curves obtained in the tensile testing of the computational samples.

The atomic-scale processes occurring during the mechanical deformation and fracture of sample CF2 are investigated by following the temporal and spatial evolution of three local characteristics of the

computational systems during the deformation. The normal atomic-level stress [70] in the direction parallel to the axis of the fiber, σ_{xx}, is calculated for all atoms using the average atomic volume in the system of 11.15 Å^3 (total volume of the CF2 system divided by the number of atoms in the system). The atomic stresses are averaged over neighboring atoms located within a cutoff distance of 9 Å. The atomic axial strain, ε_{xx}, is calculated from the Green-Lagrangian strain tensor $\boldsymbol{\varepsilon} = \frac{1}{2}(\boldsymbol{J}^T\boldsymbol{J} - \boldsymbol{I})$. Here, $\boldsymbol{J}$ is the atomic deformation gradient tensor [71–73] defined so that the mean-square difference between the actual displacements of neighboring atoms j relative to a central atom i and the relative displacements described by a linear local strain field $\boldsymbol{J}$, $\sum_{j\in n_i}\left|\boldsymbol{r}_j\,(t) - \boldsymbol{r}_i\,(t) - \boldsymbol{J}\bullet(\boldsymbol{r}_j\,(t-\Delta t) - \boldsymbol{r}_i\,(t-\Delta t))\right|^2$, is minimized. In this expression, $\boldsymbol{r}$ refers to atomic positions, i and j denote the central atom and its neighbors, respectively, n_i is the number of neighbors of atom i within a cutoff distance of 4 Å, t is the current time, and $(t-\Delta t)$ is the reference time chosen as the start of tensile testing. The minimum square displacement difference, D^2_{min}, measures the non-affine atomic displacements and can be regarded as an indicator of irreversible atomic rearrangements associated with plastic deformation.

3. Results and discussion

3.1. Structure of CF computational samples

The results of the structural characterization of the four CF computational samples are summarized in Table 2. In all samples, the dominant hybridization state of carbon atoms is sp^2 (92–93%), with most of these atoms arranged into graphitic/turbostratic carbon sheets, as reflected by the large fraction (85–90%) of 6-member rings identified by the carbon ring analysis. Most of the non-6-member rings are not related to the internal defects in the graphene sheets, such as vacancies, Stone-Wales defects, dislocations, and grain boundaries [74,75], but are largely found in disordered interfacial regions separating the graphitic and turbostratic domains. The degree of graphitization (fraction of carbon atoms that belong to the low-energy graphitic regions) exhibits a more significant variability across the samples. The samples CF3 and CF4, prepared with finite dehydrogenation rates, have ~33% smaller fraction of graphitic phase as compared to the other two samples, where the carbonization was done by simultaneous removal of the armchair/zigzag hydrogen atoms. As can be seen from the snapshots shown in the left panels of Fig. 2, where the low-energy atoms with local graphitic environment are colored blue, the graphitic phase is present in the form of small regions scattered throughout the samples. The graphitic regions are substantially larger in samples CF1 and CF2 as compared to samples CF3 and CF4, which is consistent with the higher values of the degree of graphitization and fraction of 6-member rings listed for these samples in Table 2.

In experiments, the sizes and shapes of the graphitic regions, as well as the degree of their alignment along the fiber axis, are commonly characterized by extracting the interlayer spacing, d_{002}, the thickness of the graphitic domains in the direction normal to the stacking of graphitic planes, L_c, and the lateral extent of ordering along the graphitic planes, L_a, from X-ray diffraction measurements [12,16–19,22,43,49,76]. To establish a direct link to the experimental data, the angularly averaged ("powder") diffraction profiles are calculated for the four computational samples, Fig. 3a, and are used for evaluation of d_{002}, L_c, and L_a.

The values of the average interplanar spacing d_{002} obtained for the computational samples from the diffraction profiles, Table 2, are within the range of interplanar distances evaluated from HRTEM image analysis for "mature" turbostratic carbon [63] and are at the higher end of the range of values obtained from diffraction measurements for PAN-based carbon-fibers [3,12,18,49,77,78]. In particular, the value of $d_{002} = 0.367$ nm obtained for CF2 is close to $d_{002} = 0.364$ nm reported for a CF manufactured from a very high molecular weight PAN precursor [3] and $d_{002} = 0.366$ nm measured for one of the commercial PAN-based CFs in Ref. [78], with both of these CFs featuring small sizes of the crystalline domains. The interplanar spacing d_{002} is known to shift towards smaller values as the temperature of carbonization increases, leading to higher degree of graphitization [79]. In general, the value of d_{002} is found to exhibit a negative correlation with the degree of graphitization f_{gr} and the size of graphitic domains L_c for a broad range of carbon materials [80]. This negative correlation is also present in data listed in Table 2 for the computational samples. The values for L_c and L_a calculated from the diffraction profiles and listed in Table 2 are slightly lower than those reported for PAN-based carbon fibers [3,12,16–18,22,49,78]. For example, the dimensions of crystalline domains are found to be in the ranges of 1.4–4.7 nm for L_c and 1.3–10 nm for L_a in Ref. [17], 1.3–1.8 nm for L_c and 3.9–6.2 nm for L_a in Ref. [3], 2.1–2.6 nm for L_c and 2.3–4.6 nm for L_a in Ref. [78]. The dimensions of crystalline domains in the computational samples range from 0.92 to 1 nm for L_c and from 1.69 to 2.05 nm for L_a, which is consistent with the visual inspection of the computational samples shown in Fig. 2, where the low-energy graphitic regions do not extend beyond several planes in thickness and a dozen of graphene unit cells in the lateral directions.

The presence of the orientational order in CF structures can be characterized by considering 2D diffraction patterns, such as the ones calculated for computational sample CF2 and shown in Fig. 3b and c. The diffraction pattern shown in Fig. 3b for the $Q_z - Q_x$ cross-section of the reciprocal space reflects the preferential alignment of carbon planes along the fiber axis. The distinct (002) and (00 $\bar{2}$) peaks located along the horizonal axis, i.e., perpendicular to the vertical fiber axis, are similar to those obtained in wide-angle x-ray diffraction measurements performed for polyethylene-derived CFs in Ref. [19]. Noticeable modulation of the intensity on the (10) ring in Fig. 3b resembles the one observed in Ref. [76], where it is attributed to the preferrable orientation of carbon hexagons, so that their corners are oriented towards the direction of the fiber axis. Similar to the experiments, the peaks combining in-plane ($h\,k$) and out-of-plane (0 0 l) indices characteristic of 3D graphitic ordering [79] are absent from the calculated diffraction patterns. The only ordering revealed by the calculated 2D diffraction patterns is the alignment of the turbostratically stacked carbon planes along the CF axis, with the characteristic dimensions of local structural ordering described by parameters L_c and L_a.

The extent of the alignment of the ordered domains in CF structures along the axis of the fiber is commonly described by the orientation parameter $<\cos^2\varphi>$ [18,19] that can be obtained from the azimuthal variation of (020) peak intensity, $I(\varphi)$ in the $Q_y - Q_x$ cross-section of the reciprocal space [19]:

Table 2
Structural characterization of the four CF computational samples generated with different compression levels and dehydrogenation rates. The structural parameters are calculated for systems relaxed in NPT MD simulations prior to the tensile deformation.

	sp (%)	sp^2 (%)	sp^3 (%)	Degree of graphitization (%)	Fraction of 6-member rings (%)	Volume fraction of voids (%)	HOF	d_{002} spacing (nm)	L_c (nm)	L_a (nm)	$<\cos^2\varphi>$
CF1	3.44	93.28	3.28	17.9	89.2	12.2	−0.395	0.368	0.99	1.98	0.065
CF2	3.21	93.38	3.41	18.3	89.0	9.3	−0.397	0.367	1.00	2.05	0.055
CF3	3.70	92.57	3.72	12.2	86.6	11.1	−0.395	0.378	0.92	1.78	0.067
CF4	3.53	92.56	3.91	11.7	85.7	10.4	−0.399	0.375	0.94	1.69	0.057

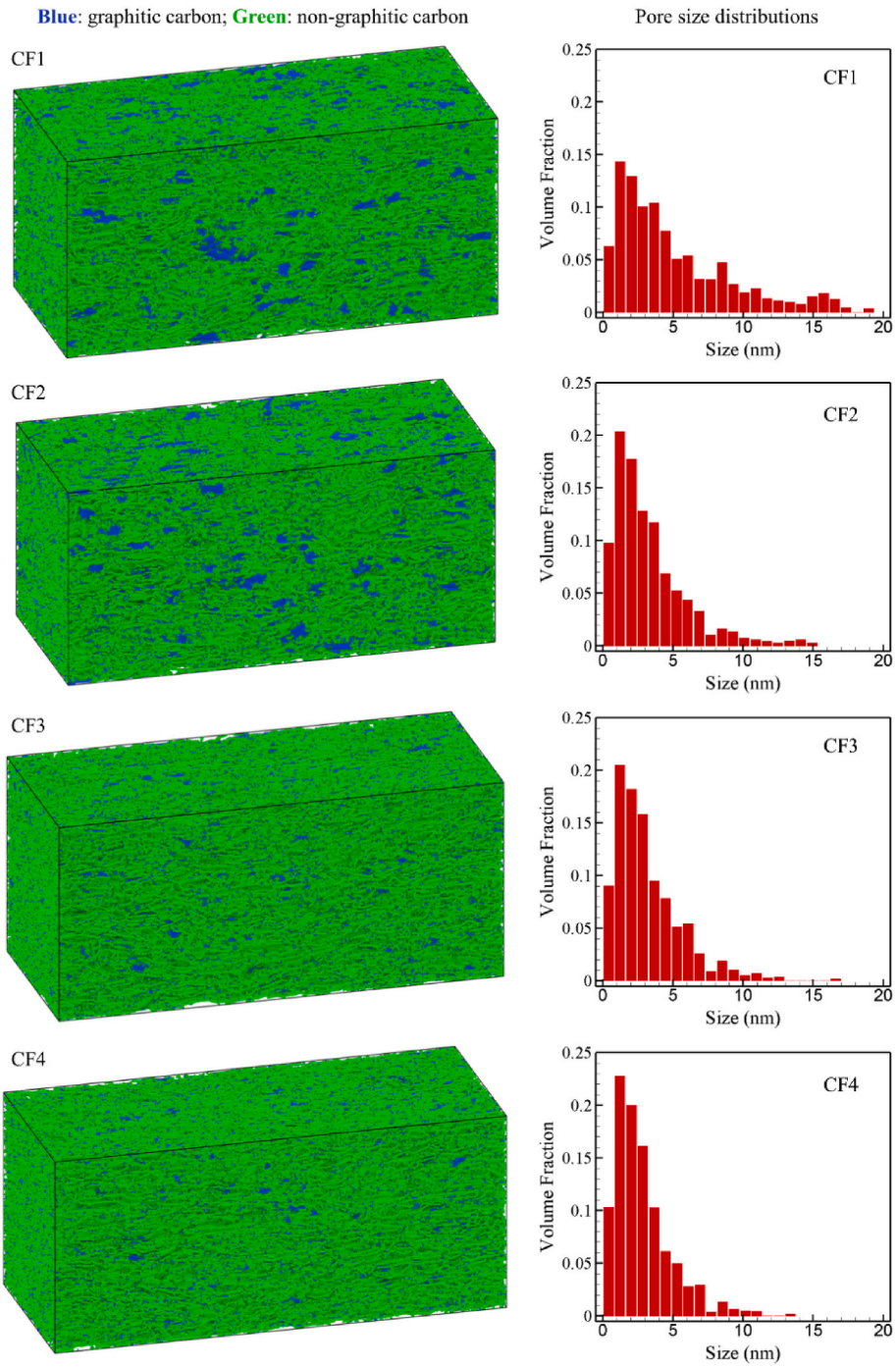

Fig. 2. Snapshots of CF microstructures with atoms that belong to graphitic regions colored blue (left panels) and the pore size distributions obtained by binning the pores based on their size with a bin width of ~0.8 nm (right panels). The pores tend to have elongated shapes, and the size of a pores is defined as the length of the longest line that can be drawn within the pore without crossing its boundaries. (A colour version of this figure can be viewed online.)

$$< \cos^2 \varphi >= \frac{\int_0^{\pi/2} I(\varphi)\cos^2 \varphi \sin \varphi d\varphi}{\int_0^{\pi/2} I(\varphi)\sin \varphi \, d\varphi} \quad (1)$$

The values for $<\cos^2\varphi>$ listed for the four computational samples in Table 2 are calculated using the procedure described in Ref. [19]. First, the $Q_y - Q_x$ cross sections of the scattering intensity in the vicinity of (020) peak position was integrated in the radial direction over an integration window with width of $2\Delta Q$, where ΔQ is FWHM of the peak in the radial direction. As a result, we obtain a distribution of normalized intensity over the azimuthal angle, $I(\varphi)$, with two distinct peaks. Before the final integration using Eq. (1), we subtract a background for $I(\varphi)$, as discussed in Ref. [19]. The values of $<\cos^2\varphi>$ are calculated for (020) and $(0\bar{2}\ 0)$ peaks, and the average between the two is taken as the final result listed in Table 2.

The relatively small values of $<\cos^2\varphi>$, ranging from 0.055 for CF2 to 0.067 for CF3, indicate a high degree of structural alignment along the fiber axes in the computational samples (perfect alignment corresponds to zero value of $<\cos^2\varphi>$) and are consistent with the range of values

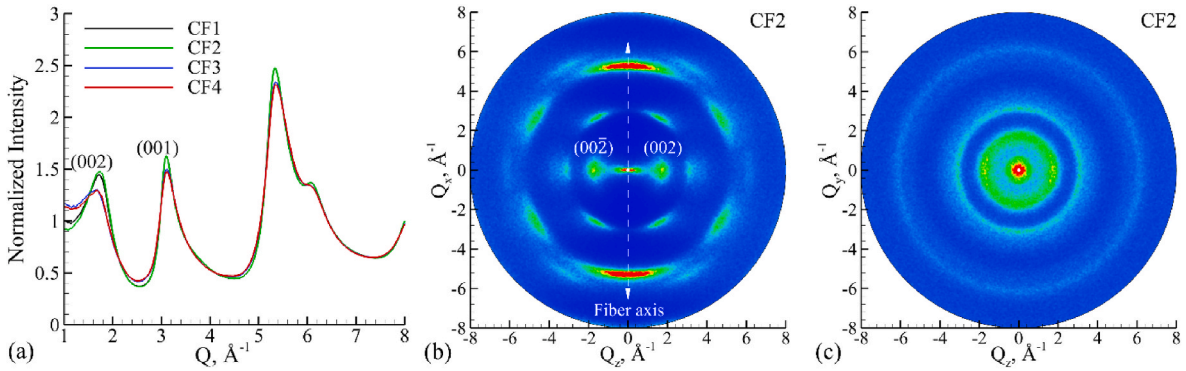

Fig. 3. Angularly averaged diffraction profiles calculated for the four computational samples (a) and 2D diffraction patterns calculated for sample CF2 in $Q_z - Q_x$ (b) and $Q_z - Q_y$ (c) planes in the reciprocal space. The orientation of the fiber axis is shown by the dashed vertical line in (b). (A colour version of this figure can be viewed online.)

obtained experimentally for PAN-based CFs [18,19], *e.g.*, 0.009–0.073 in Ref. [18]. The orientation parameter $<\cos^2\varphi>$ and HOF can be related to each other as $HOF = (3<\cos^2\varphi> - 1)/2$ [81]. The values of HOF obtained from the diffraction profiles are within 5% of the ones calculated directly from the structural analysis of atomic configurations and listed in Table 2. Note that the orientation parameter $<\cos^2\varphi>$ derived from diffraction data is also used in the uniform stress model relating the Young's modulus to the in-plain modulus of graphite and a modulus describing the elastic response to shear between adjacent graphitic layers [18,19,82]. While this model is suitable for CFs consisting of well-defined graphitic domains, the description of the elastic properties of more disordered nanostructures consisting of curved and folded layers of turbostratic carbon may require revisiting the assumptions of the model.

As discussed below, in sections 3.2 and 3.4, the presence of nanoscale pores, their sizes and shapes are important factors that affect the mechanical properties of CFs. The values of the total volume fraction of pores in the CF systems, listed in Table 2, are in a good quantitative agreement with the corresponding values determined for PAN-based fibers in small angle X-ray scattering (SAXS) measurements, 8–12% [76] and 3–12% [22]. The distributions of volume fractions of pores of different sizes, shown in the right panels of Fig. 2, demonstrate that in all computational samples the total porosity is mostly defined by small pores with characteristic sizes below 5 nm. The sample compressed to a lower level of pressure of 0.15 GPa prior to the carbonization, CF1, has the largest volume fraction of pores as well as the maximum pore size, although the total density of this sample is not the lowest, Table 1. For the other three samples compressed to 0.3 GPa prior to the carbonization, the porosity follows the density trend and is the lowest for sample CF2, which also has the highest density.

The nanopores present in the computational samples have highly elongated shapes [23], are aligned along the fiber axis, and have a length up to 20 nm (Fig. 2). These characteristics of the nanopores are consistent with the results of experimental X-ray diffraction probing of voids present in PAN-based CFs, where needle-like pores oriented preferentially along the fiber axis have been identified [12,43,76]. The dimensions of the experimentally observed pores, less than 5 nm in the direction perpendicular to the fiber axis [12,43,76] and 25 [43] or 30–90 nm [76] along the fiber axis, are in a reasonable agreement with the computational samples representing a small part of the CF microstructure. We note that the origin of the needle-like voids in the simulated samples is different from that suggested by the Ruland's model [76,83], where the voids appear as gaps between well-ordered graphitic ribbons undulating around the fiber axis as they pass from one graphitic domain to another. Rather, the nanovoids in the computational systems are intrinsic to the highly distorted turbostratic constituent of CFs, where the voids are naturally present within the structure featuring wrinkled and folded graphene layers. The dominant presence of axially aligned turbostratic constituent in high-strength PAN-based CFs is supported by the results of HRTEM imaging [3,12,13,16].

3.2. Stress-strain curves and mechanical properties of CF computational samples

To investigate the effect of different structural characteristics on the CF mechanical properties, MD simulations of tensile deformation are performed with the ReaxFF interatomic potential for the four CF computational samples. As described in Section 2.3, the CF samples are stretched along the fiber axis with an engineering strain rate of 4×10^8 s^{-1} until the fracture occurs. The stress-strain curves and atomic configurations of fractured CFs are shown in Fig. 4. The shapes of the stress-strain curves exhibit a gradual stiffening of the elastic response of the CFs with increasing strain and an abrupt drop of the stress at the fracture strain, which is characteristic of brittle fracture. The stiffening in the elastic regime can be attributed to the mostly reversible structural changes in the CF nanostructure leading to an effective enhancement of the Young's modulus at higher values of the tensile strain. A similar behavior has been observed in simulations of carbon nanofibers with diameters of ~20 nm, where the elastic response of the nanofiber is described by two values of Young's modulus calculated for the low- and high-strain stages of the tensile deformation [28]. In the present paper, in Table 3 we provide the effective Young's moduli of CFs fitted for the strain ranges extending up to the fracture strains. We note, however, that the initial elastic response at strain values up to 2% is characterized by lower Young's moduli ranging from 205 to 225 GPa.

The snapshots of atomic configurations in Fig. 4a are shown for strain levels exceeding the fracture strain by ~3%. By the time these levels of strain are reached, the cracks nucleated in regions of local stress concentration fully expand through the cross-sections of the computational samples. The fracture surfaces are still connected by several bridges consisting of narrow graphene nanoribbons and chains of carbon atoms (carbyne), although these bridges do not support any stress and readily break upon further extension of the systems. Note that one of the implications of the 3D periodic boundary conditions applied in the simulations is that the fracture leads to an effective splitting of the CFs into segments with sizes similar to those of the original computational systems. The sudden release of the tensile stress upon the brittle fracture triggers elastic vibrations in the CF segments. Since at the strain rate of 4×10^8 s^{-1} the engineering strain is increasing with time by 1% per 25 ps, the elastic vibrations appear in the stress-strain curves as gradually attenuating oscillations above the fracture strain. These oscillations should not be considered as parts of true stress-strain dependences but are artifacts of mapping the strain rate to time. The period of the oscillations corresponds to the time needed for a stress wave to path back and forth along the *x* direction in the segments of the computational CFs produced by the fracture.

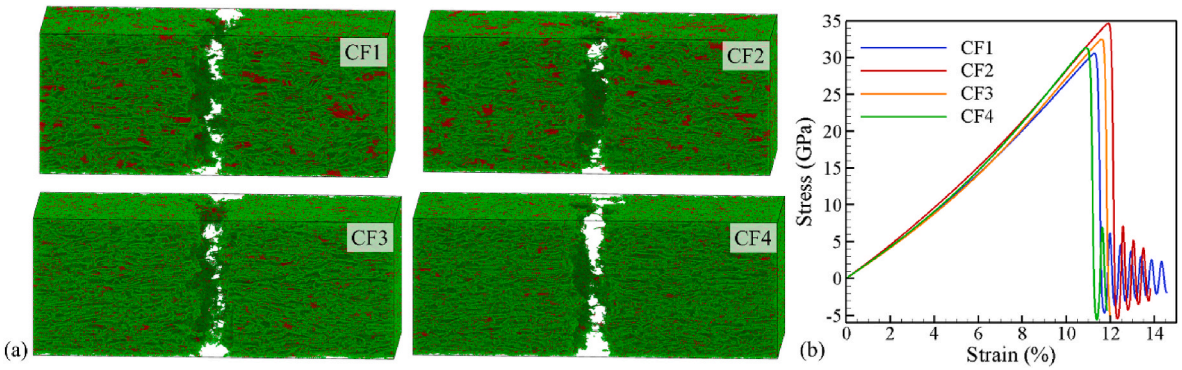

Fig. 4. Snapshots of atomic configurations of fractured CFs (a) and stress-strain curves (b) predicted in MD simulations of tensile deformation of the four carbon fiber samples. The snapshots are shown for strain levels exceeding the fracture strain by ~3%, namely, 11.6% for CF1, 12.2% for CF2, 11.9% CF3, and 11.3% for CF4. The atoms that belong to the low-energy graphitic regions in the initial samples (prior to the deformation) are colored red, while non-graphitic carbon atoms are colored green. The systems are shifted along the axes of CFs (horizontal direction) so that the locations where the fracture occurs are aligned with the centers of the snapshots. (A colour version of this figure can be viewed online.)

Table 3
Mechanical properties of the four CF computational samples predicted in MD simulations of tensile testing.

	Young's modulus (GPa)	Tensile strength (GPa)	Fracture strain (%)
CF1	266.6	30.6	11.3
CF2	287.4	34.6	11.9
CF3	275.6	32.5	11.6
CF4	280.7	31.3	10.9

As can be seen from Table 3, despite the variation of structural characteristics across the computational samples, the mechanical properties of the four CFs are rather similar. The values of the effective Young's modulus predicted in the simulations range from 267 to 287 GPa, which is within the broad range of experimental values reported for PAN-based fibers, ~200–600 GPa [1,3,9,12,13,15–17,49], while the Young's moduli calculated based on the initial part of the stress-strain curves, 205–225 GPa, are consistent with those estimated for the "disordered" (non-graphitic) regions of CFs in Ref. [17], 159–212 GPa. The latter agreement is particularly notable, since the degree of graphitization is relatively low in the computational samples (see Table 2) and the mechanical properties of the fibers are expected to be largely controlled by properties of the dominant disordered (highly distorted turbostratic layers) constituent of the fibers. The comparison between the computational samples reveals a negative correlation between the effective Young's modulus and the volume fraction of pores (*cf*. Tables 2 and 3), which may be attributed to the softening effect of nanoscale pores distributed through the system.

In contrast to the Young's modulus, the values of the tensile strength predicted in the MD simulations, ~30–35 GPa, are about three times higher than the record values of ~13 GPa reported for PAN-based CFs [16,17], and even further away from the tensile strength of commercially available CFs, typically ranging between 2 and 7 GPa [3,9,12,13,15,16,49]. The high tensile strength of the computational samples can be partially attributed to the absence of surface defects and internal flaws causing the stress concentration and initiation of fracture in experimental samples [3,12–16,29,30]. Indeed, the extrapolation of the gauge length dependence of the tensile strength measured for PAN-based CFs to the defect-free nanoscale range in Ref. [16] yielded an estimate of the limiting tensile strength as high as 20.9 GPa. Similarly, the inherent tensile strength of the disordered CF constituent of up to 19.5 GPa was estimated based on the results of loop test measurements of the tensile strength of commercially available PAN-based CFs [17]. These limiting values are comparable to the tensile strength predicted in the simulations. Moreover, an additional important factor responsible for enhancing the tensile strength and fracture strain in the computational samples is the absence of large graphitic domains and overall nanoscale uniformity of the computational samples, which minimizes the stiffness mismatch between the structural elements of the CF nanostructure and reduces the stress concentration. The atomic-scale analysis of the mechanical deformation discussed below, in Section 3.3, reveals the ability of the CF nanostructure, largely consisting of curved and folded layers of turbostratic carbon, to exhibit continuous nanoscale load redistribution during the deformation. This adaptive mechanical behavior is found to be the key factor that enables the deformation up to strain levels as high as ~11%.

Before turning to the detailed analysis of processes leading to the internal redistribution of stresses during the deformation, we consider the evolution of the distributions of mechanical characteristics along the fiber axis. The distributions, shown for the four CF samples in Fig. 5, are calculated by dividing the system into ~1-nm-thick slices along the fiber axis and averaging the atomic axial stress σ_{xx}, standard deviation of the atomic axial stress SD(σ_{xx}), axial atomic strain ε_{xx}, standard deviation of the axial atomic strain SD(ε_{xx}), and the minimum square displacement difference D^2_{min} within each slice. For easier comparison among the samples and better visualization, the systems are shifted along the fiber axes, so that the central parts of the systems, $x \approx 0$ nm, correspond to location where the fracture takes place.

As expected, the mechanical balance is maintained during the deformation, and the axial atomic stress averaged over the cross-sectional slices is evenly distributed along the axes of the CFs. The values averaged over the slices are consistent with the average stress in the entire system marked in Fig. 5a by the dashed lines. The nanoscale heterogeneity of the CF structures, however, leads to the variations of atomic stress within the CF cross-sections, which can be quantified by the standard deviation of the axial stress shown in Fig. 5b. The standard deviation is substantial, from 6 to 8 GPa, even in the initial mechanically relaxed sample, which reflects the large spread in the magnitudes of atomic-level internal stresses characteristic of systems with short and medium range order, *e.g.*, amorphous materials [84]. The standard deviations of the cross-sectional distributions of atomic stress increase with increasing system strain, as does the slice-to-slice variation of the standard deviation. The samples CF1 and CF4 exhibit the highest initial values of SD(σ_{xx}) and the largest slice-to-slice variations of the standard deviation. This observation suggests the higher levels of heterogeneity of the internal structure and stress localization, which may be related to the lower strength and fracture strain of these two samples, Table 3. As can be seen from Fig. 5c–e, the regions of fracture initiation share a common feature of a gradual pileup of the atomic strain, standard deviation of atomic strain, and non-affine atomic displacement for all CF samples. The value of D^2_{min} that reflects the nonuniformity of local atomic displacements appears to be the most sensitive indicator of the

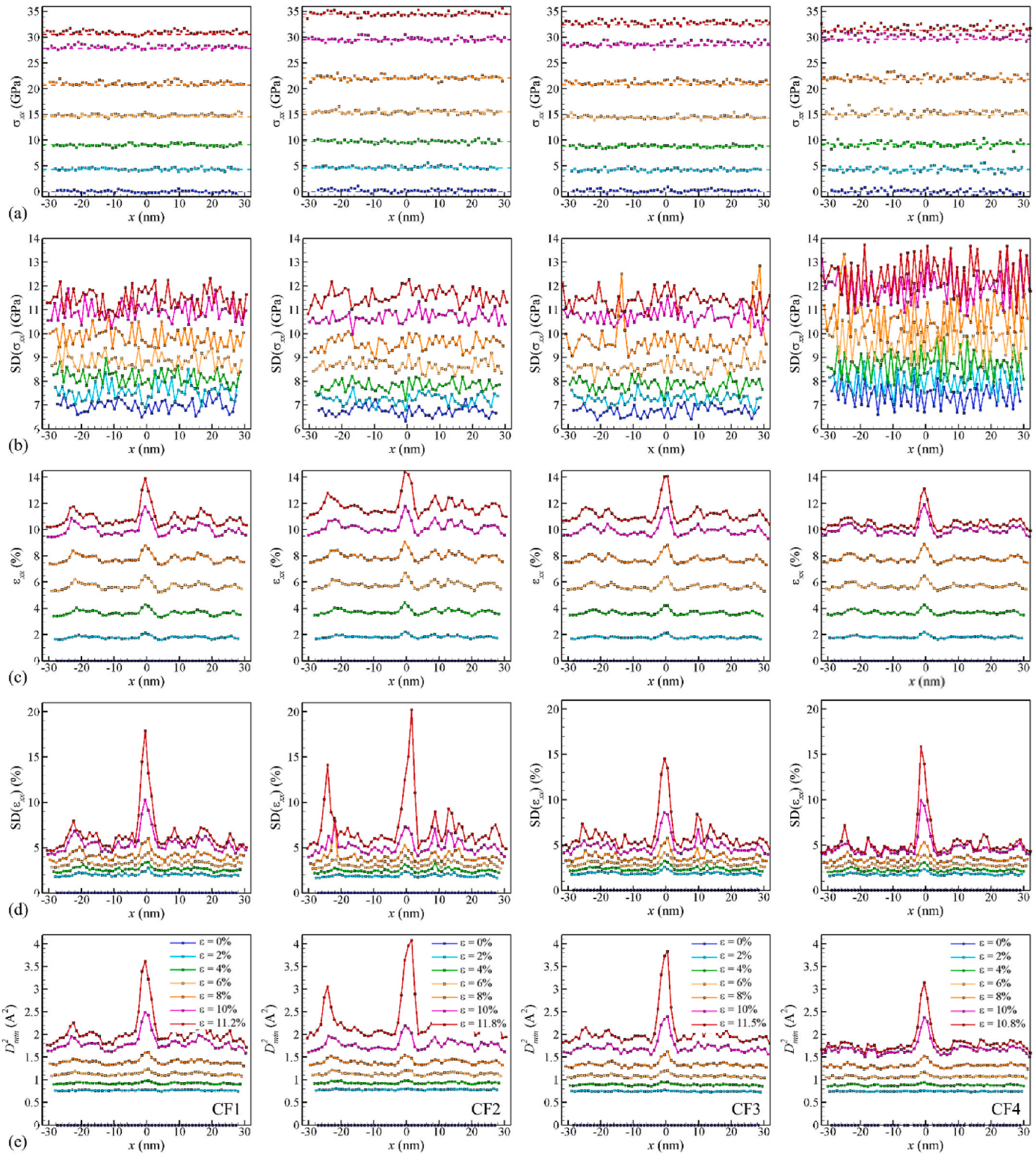

Fig. 5. Distribution of axial atomic stress σ_{xx} (a), standard deviation of the atomic stress SD(σ_{xx}) (b), axial atomic strain ε_{xx} (c), standard deviation of the atomic strain SD(ε_{xx}) (d), and the minimum square displacement difference D^2_{min} (e) along the fiber axis (x-axis) at different levels of system strain ε predicted in MD simulations of the tensile testing of the four CF samples. The systems are divided into ~1-nm-thick slices along the fiber axis, and the data points show the values averaged over the slices. The dashed lines in (a) correspond to the stress values calculated for the whole system. Similar to the snapshots in Fig. 4a, all systems are shifted along the fiber axes, so that the fracture is initiated in the central parts of the systems, at $x \approx 0$ nm. The legends for the levels of strain are provided in the bottom set of the panels.

onset of irreversible atomic rearrangements leading to the initiation of fracture.

The analysis of the characteristics of the mechanical deformation averaged over cross-sectional slices shown in Fig. 5 highlights the importance of the nanoscale variations of atomic stress and yields the general picture of the localization of irreversible deformation responsible for the eventual fracture of the computational CFs. To uncover the mechanisms responsible for the mechanical deformation and fracture, however, a more detailed investigation of processes occurring at the level of nanoscale elements of the CF structures is needed. Such analysis is performed in the next section for the computational sample CF2, which has the highest density (Table 1), is characterized by the highest degree of graphitization and the lowest volume fraction of nanoscale voids (Table 2), and exhibits the highest tensile strength and fracture strain (Table 3). The results for the other three CF samples are qualitatively similar and are not presented to avoid redundant discussions.

3.3. Nanoscale mechanisms of the mechanical deformation and fracture

As the first step in the analysis the nanoscale mechanisms of the tensile deformation and fracture, we consider the evolution of the stress distribution in a 3-nm-thick slice cut from the computational sample CF2 along the *x*-*y* plane. The stress distributions are shown in Fig. 6 for five consecutive levels of strain ranging from 2 to 10%. One striking characteristic apparent from the visual inspection of Fig. 6 is the pronounced nanoscale heterogeneity of the stress distributions. Some regions are relaxed with nearly zero stress, while other regions hold stress that is several times higher than the average stress in the whole system. It is this heterogeneity of stress distribution that is responsible for the large values of the standard deviation of the atomic stress within slices of CF in Fig. 5b. With increasing level of deformation, the stress distribution remains highly heterogeneous, but the ratio of the maximum stress to the overall average stress value is reduced. Interestingly, even at the highest strain of 10%, there are some zero-stress regions in the CF that do not support any load. Another important observation from Fig. 6 is that the location of high- and low-stress regions is constantly changing in the course of the deformation, supporting the notion that the large fracture strain predicted in the simulations is largely defined by the ability of the CF nanostructures to adapt to the increasing strain through the nanoscale load redistribution.

Thus, the results of the visual inspection of the stress distributions provided in Fig. 6 suggest the following further steps in the analysis of the mechanisms of the deformation and fracture. The correlations between the local structural and mechanical characteristics of the CF are examined first. Next, the stress localization and structural rearrangements leading to the onset of fracture are considered with atomic-scale resolution. Finally, the evolution of the mesoscopic continuous network of regions supporting the mechanical load during the deformation is studied, and the results are used for explaining the ability of the disordered turbostratic CF structure to support the stress levels up to 30–35 GPa, comparable to the strength of polycrystalline graphene [85].

To establish the correlations between the local response to the mechanical deformation (atomic strain ε_{xx}, atomic stress σ_{xx}, and D^2_{min}) and local characteristics of the nanostructure (density ρ, fractions of carbon atoms in sp, sp^2 and sp^3 hybridization states f_{sp}, f_{sp2}, and f_{sp3}, atomic potential energy E_p, degree of graphitization f_{gr}, and fraction of 6-member rings $f_{6\text{-ring}}$) we divide the computational sample CF2 into 36 × 16 × 16 cells and average the structural and mechanical characteristics in each cell. The dimensions of the rectangular cells are changing during the tensile deformation, from 1.5 to 1.7 nm in *x* direction, from 1.5 to 1.4 nm in *y* direction, and from 1.6 to 1.5 nm in *z* direction. The Pearson correlation coefficients are then calculated for different pairs of structural and mechanical characteristics based on the average values calculated for the 9216 cells at several levels of the mechanical deformation. The values of the correlation coefficients reflect the degree of linear correlation between the local structural and mechanical characteristics, with 1 and -1 corresponding to perfect positive or negative correlations, and values around zero pointing to the absence of the linear correlation.

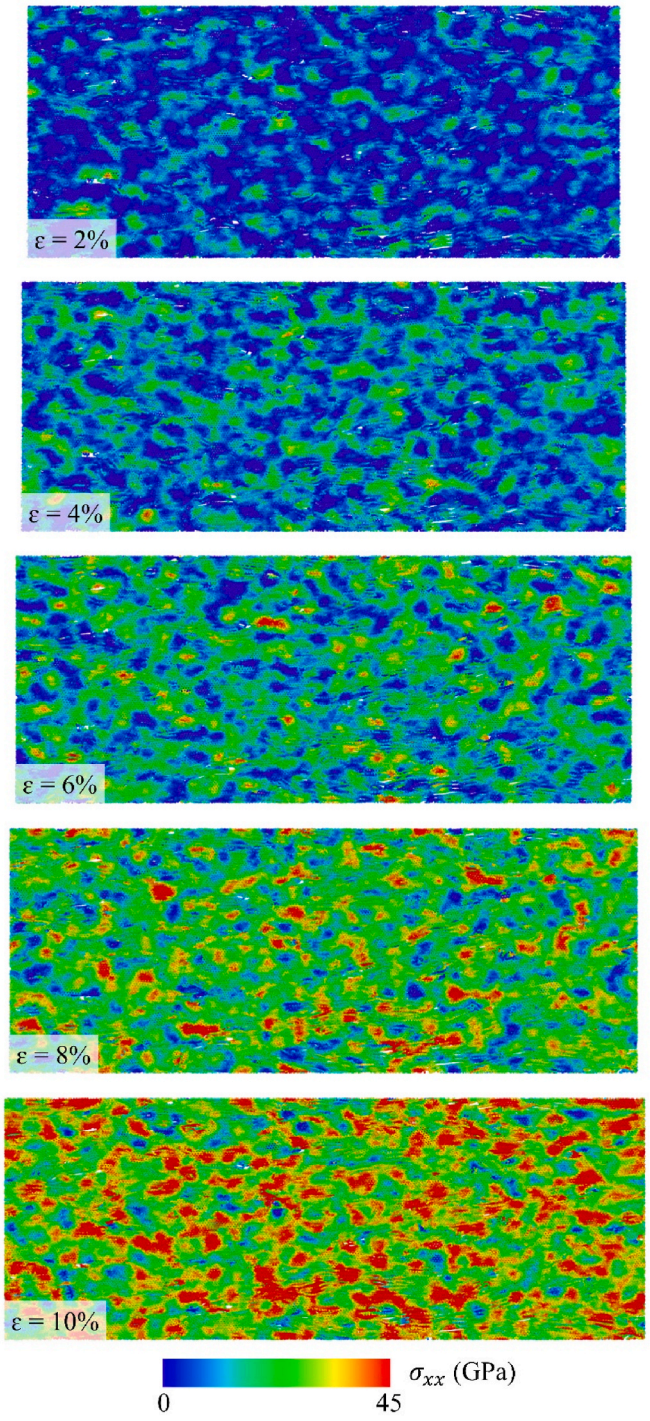

Fig. 6. Evolution of the stress distribution predicted in MD simulation of tensile deformation of the sample CF2. The stress distributions are shown for 3-nm-thick slices cut from the computational system along a plane parallel to the axis of the fiber (*x*-*y* plane). The values of strain are marked on the panels. The atoms are colored based on the local atomic stress averaged over neighboring atoms located within a cutoff distance of 9 Å. (A colour version of this figure can be viewed online.)

The correlation coefficients between local mechanical and structural characteristics calculated for the CF2 sample strained to ε = 10.4% are

shown in Fig. 7 in the form of a histogram. For each structural characteristic, the sizes of the three histogram bins correspond to the values of the correlation coefficients for ε_{xx}, σ_{xx}, and D^2_{min}. As can be seen from the histogram, the cells that support higher stress tend to have higher density, higher fractions of sp^2 carbon and 6-member rings, as well as higher level of graphitization. The high values of the local strain and minimum square displacement difference, on the other hand, are positively correlated with the enhanced fraction of sp carbon and elevated potential energy. We note that most of the atoms with sp hybridization and high potential energy are not produced by the bond breakage during the deformation but are present in the initial structure of the CF. Indeed, the correlations shown for these local parameters in Fig. 7 are also present at lower values of system strain ε. The correlation between the mechanical properties and the fraction of sp^3 carbon atoms is weak, which may be related to the small fraction of such atoms (Table 2) that are not concentrated in distinct regions but participate in crosslinks between the graphitic/turbostratic layers. Generally, the correlation coefficients of any structural characteristic with the local stress have opposite signs to those with the local strain or minimum square displacement difference.

The quantitative analysis of the correlations between the structural and mechanical properties reveals the important implications of the structural heterogeneity on the local stress and strain distributions. However, it does not provide direct information on the stress localization and structural rearrangements leading to the onset of fracture. To investigate the atomic-scale processes responsible for the initiation of fracture with atomic resolution, we consider two cross-sections of the atomic configuration of sample CF2 that go through the location where fracture is initiated. The first cross-section is made normal to the axis of the fiber (*y*-*z* plane) and is shown in Fig. 8 for a strain of ε = 11.84%, just below the fracture strain. The second cross-section is made parallel to the axis of the fiber (*x*-*z* plane) and is shown in Fig. 9 for several levels of strain corresponding to the initiation of fracture, from 11.79% to 11.95%.

The cross-sectional distribution of the atomic stress, shown in Fig. 8a, reveals several regions of strong stress localization, with red structural elements holding stress that is more than twice higher than the average stress in the whole system. The region where the fracture is initiated upon further deformation (marked by the black ovals), however, does not correspond to the brightest or largest red spot in the stress distribution. The panels shown in Fig. 8b and c, however, demonstrate that this region features large variations of strain and non-affine displacements. This observation suggests that the fracture is initiated in a region featuring a combination of stiffer and more compliant elements of the nanostructure. Analysis of the panels showing the distribution of hybridization status of carbon atoms, graphitic carbon atoms, and 6-member rings, Fig. 8d–f, indicates that the region where fracture starts is characterized by a substantial fraction of sp carbon, a small degree of graphitization, and a relatively low fraction of 6-member rings. These structural characteristics are consistent with the elevated local strain and non-affine displacement, as suggested by the results of correlation analysis illustrated by Fig. 7.

The atomic-scale picture of the initiation of the fracture process is provided in Fig. 9, where side-views of atomic configurations colored by atomic stress (Fig. 9a), atomic strain (Fig. 9b), and presence of chemical bonds broken or newly formed during the mechanical deformation (Fig. 9c) are shown for strain levels below and above the fracture strain. The events of bond scission and formation of new bonds are identified from changes in hybridization state of carbon atoms during the deformation. At strains below the onset of fracture, at $\varepsilon < 11.9\%$, the region outlined by the white ovals is characterized by a moderate low level of atomic strain and a small number of broken bonds. The strain and the number of broken bonds, however, are much higher in the immediate vicinity of this region, suggesting the likelihood of the load redistribution to the outlined region. Indeed, at $\varepsilon > 11.8\%$, the stress rapidly builds up in the region outlined by the white oval, leading to the bond scission within the stress-holding element of the nanostructure and formation of a critical nano-crack at $\varepsilon \approx 11.9\%$. The emergence and propagation of the nano-crack is manifested by the appearance of many broken chemical bonds (blue dots in Fig. 9c), the rapid relaxation of local stress (expansion of the blue region in Fig. 9a), and accumulation of local strain (merger and growth of red regions in Fig. 9b) that can be seen in the snapshots shown for $\varepsilon = 11.95\%$. The subsequent rapid growth of the nano-crack leads to the sudden release of stress in the whole sample characteristic of brittle fracture, Fig. 4b.

The analysis of the simulation results provided above reveals two seemingly contradictory trends. On one hand, the nonuniform stress distribution in the sample cross-sections shown in Fig. 6 and the correlations between local mechanical and structural characteristics illustrated by Fig. 7 suggest that the CF nanostructure can be thought of as a mixture of strong/stiff and soft, more compliant nanoscale regions. The strong regions are capable of supporting higher stress and tend to have higher density, higher fraction of sp^2 carbon and 6-member rings, as well as higher level of graphitization. The softer regions are more deformable (higher values of ε_{xx} and D^2_{min}) and are characterized by higher potential energy and elevated fraction of sp carbon. On the other

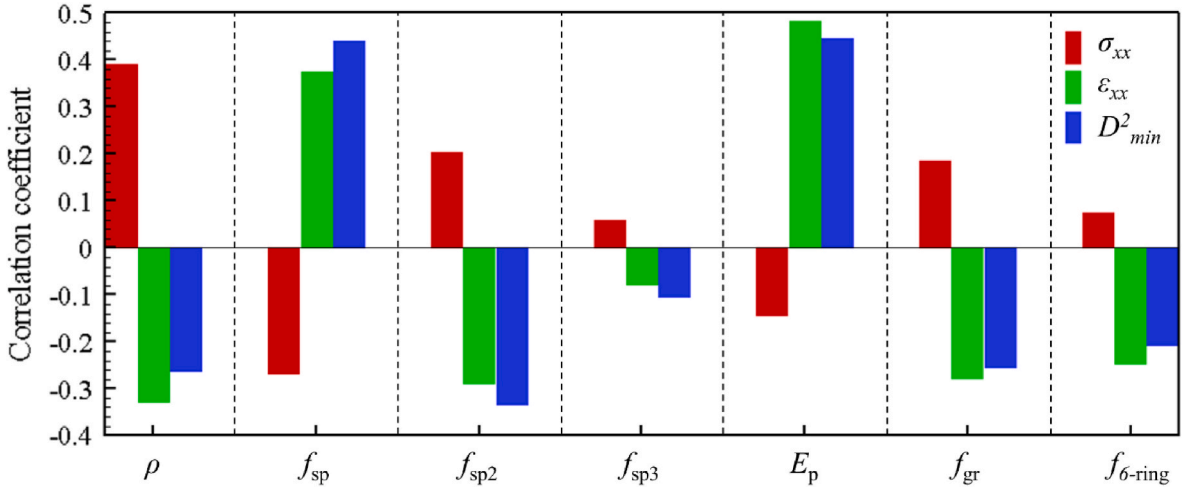

Fig. 7. Histogram showing the correlation coefficients between local structural characteristics (ρ, f_{sp}, f_{sp2}, f_{sp3}, E_p, f_{gr}, and $f_{6\text{-ring}}$) and local mechanical response to the deformation (ε_{xx}, σ_{xx}, and D^2_{min}) calculated for sample CF2 at $\varepsilon = 10.4\%$. The system is divided into 36 × 16 × 16 cells, and the structural and mechanical characteristics are calculated for each cell.

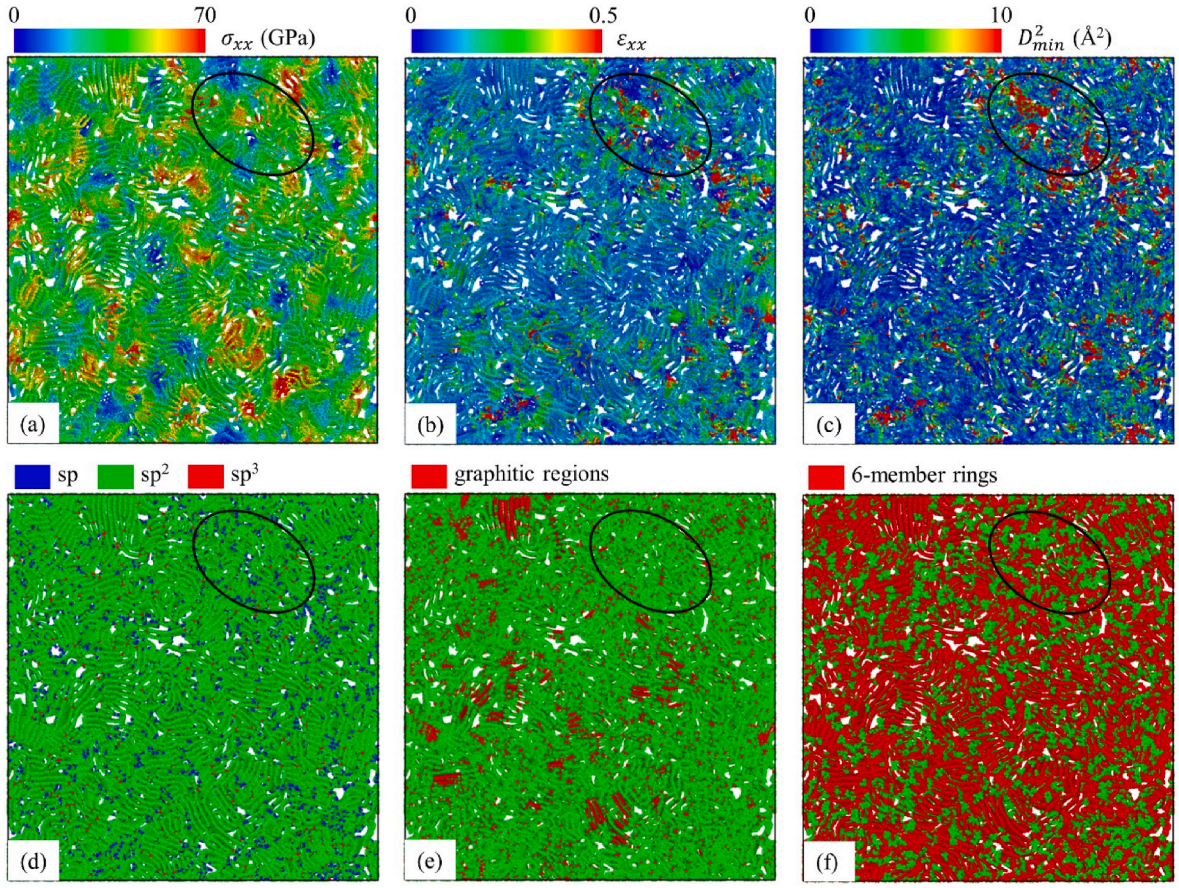

Fig. 8. Snapshot of a 3-nm-thick slice cut from the computational sample CF2 along plane normal to the axis of the fiber (*y*-*z* plane). The fiber is strained to $\varepsilon = 11.84\%$, slightly below the onset of fracture. The cut is made through a location where the fracture is initiated, and the black ovals outline the central part of the damage accumulation region where a critical crack is generated upon further deformation. The atoms are colored according to the atomic stress σ_{xx} (a), atomic strain ε_{xx} (b), minimum square displacement difference D^2_{min} (c), hybridization state (d), association with graphitic structure (e) and 6-member rings (f). In (a), the atoms are colored based on the local atomic stress averaged over neighboring atoms located within a cutoff distance of 9 Å. In (e), atoms that belong to the graphitic phase are colored red. In (f), the 6-member rings are colored red, and the individual rings are plotted based on the average atomic positions forming the ring.

hand, a notion of a pre-existing skeleton of strong regions that supports most of the load and is surrounded by a softer matrix is inconsistent with the frame-to-frame variation of the stress distribution in Fig. 6 as well as the sudden (within the final 0.1% of the deformation) local spike in the stress level leading to the fracture onset in Fig. 9. This transient/flickering nature of the stress distribution calls for an additional analysis aimed at providing insights into the mechanisms responsible for the impressive load-bearing ability of the disordered nanostructure consisting of curved and folded layers of turbostratic carbon.

In general, one may expect that the strong regions supporting high stresses in the CF nanostructure are connected into a continuous network percolating through the whole system and holding the mechanical load during the deformation. To identify the high-stress percolating network, we perform a cluster analysis connecting the neighboring atoms that hold a value of the atomic axial stress σ_{xx} above a certain threshold level into clusters. Each pair of high-stress atoms separated from each other by less than 2 Å is assigned to the same cluster. For high values of the stress threshold, the cluster analysis yields only separated clusters consisting of tens or hundreds of atoms. Decreasing the stress threshold leads to the expansion and merger of the high-stress clusters, some of which may percolate through the whole system in the axial direction. The stress threshold is adjusted until the smallest percolating cluster is produced.

The atomic configurations of the percolating clusters are shown in Fig. 10 for different strain levels prior to the fracture initiation. The left panels show 3D structures of the clusters, and the right panels show cross-sectional views of 3-nm-thick slices cut along the *y*-*z* plane from the middle of the cluster, where the fracture starts at $\varepsilon = 11.90\%$. The values of the strain level and the threshold stress leading to the formation of the percolating clusters are shown below each configuration. As deformation proceeds, the threshold stress to obtain the percolating cluster with minimum size increases and reaches the level of 43.9 GPa, about 27% above the average stress in the system, just before the onset of fracture. As can be seen from Fig. 10, some of the regions of high stress are preserved in the percolating clusters identified at different strain levels, suggesting that these regions may indeed belong to the backbone structure holding the high stress until the mechanical failure. In general, however, the percolating cluster displays a rather transient nature with its shape undergoing significant evolution during the deformation. Such behavior may be directly linked to the high resilience of the CF samples to fracture: If the percolating cluster was static, the stress would steadily build up in the cluster, leading to the brittle failure at low levels of fracture strain. The continuous nanoscale redistribution of the mechanical load, suggested by the fluid nature of the percolating cluster of high-stress regions, makes it possible for the CF structures to adapt to the increasing load and deform up to a fracture strain in excess of 10%.

The important implications of the effect of continuous nanoscale redistribution of stress during the CF deformation call for quantification of the conjectures discussed above based on the mere visual inspection of the evolution of the percolating cluster of high-stress regions. To place the discussion of the transient fluid nature of the percolating cluster of stress-holding structural elements on a solid quantitative footing, we

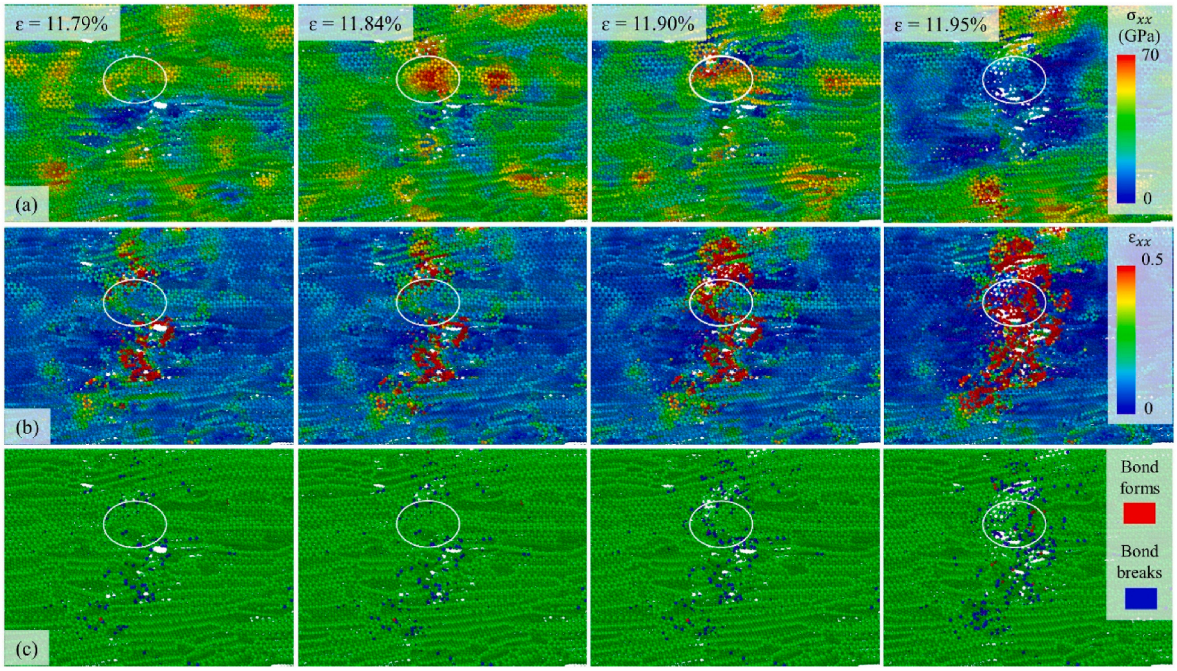

Fig. 9. Snapshots of a part of a 3-nm-thick slice cut from the computational sample CF2 along a plane parallel to the axis of the fiber (*x*-*z* plane) shown for several levels of strain, from 11.79% to 11.95%, as marked on (a). The cut is made through a location where the fracture is initiated at ε = 11.90%, and the white ovals mark the region where the final critical events of the atomic-scale stress concentration and bond scission occur, leading to the formation of a critical crack and catastrophic failure of the fiber. The atoms are colored according to the atomic stress σ_{xx} (a), atomic strain ε_{xx} (b), and the change in hybridization state of carbon atoms during the deformation (c). In (a), the atoms are colored based on the local atomic stress averaged over neighboring atoms located within a cutoff distance of 9 Å. In (c), the atoms are colored based on the change in the number of chemical bonds with respect to the initial hybridization state at ε = 0%. The atoms with higher number of bonds (bond forms), lower number of bonds (bond breaks), and unchanged hybridization are colored red, blue, and green, respectively. (A colour version of this figure can be viewed online.)

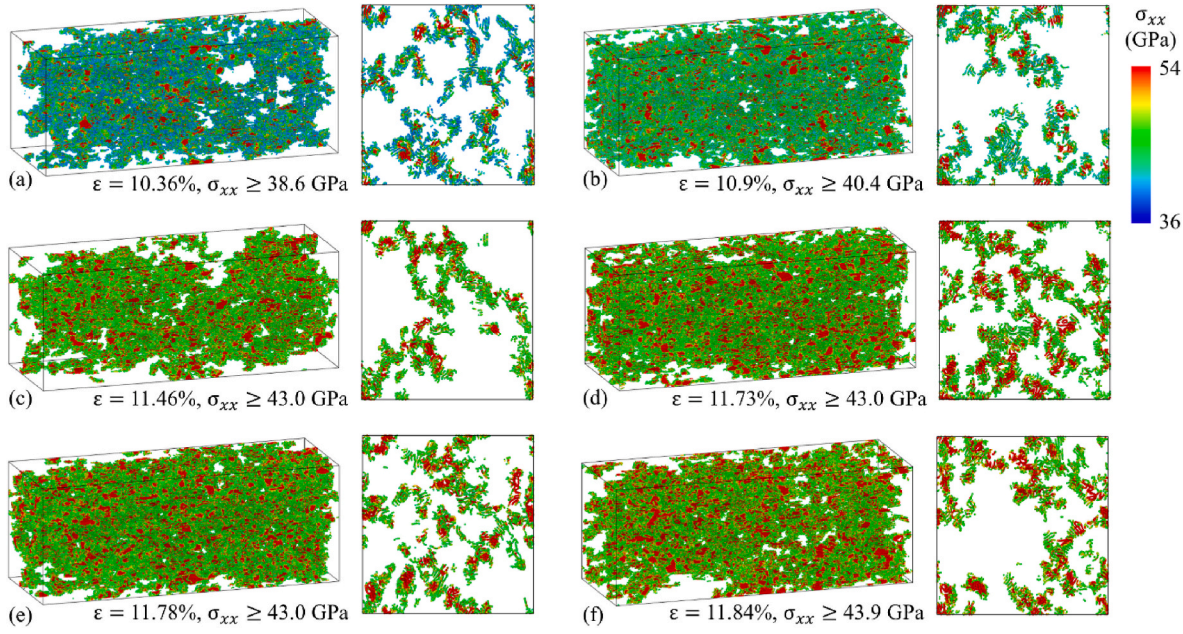

Fig. 10. Snapshots showing configurations of smallest percolation clusters of high-stress regions identified in the computational sample CF2 at different levels of strain: ε = 10.36% (a), ε = 10.9% (b), ε = 11.46% (c), ε = 11.73% (d), ε = 11.78% (e), and ε = 11.84% (f). The atoms included in the clusters are characterized by the atomic axial stress σ_{xx} exceeding the threshold levels that produce the smallest continuous clusters percolating through the systems in the axial direction. The right panels show 3-nm-thick slices cut from the percolation clusters along the fiber cross-section (*y*-*z* plane) in the middle of the fiber. The system is shifted along the fiber axis (*x*-axis) so that fracture is initiated in the central part of the system. The atoms are colored based on the local atomic stress averaged over neighboring atoms located within a cutoff distance of 9 Å. (A colour version of this figure can be viewed online.)

perform self-correlation analysis of the atomic stress and other local mechanical and structural parameters during the mechanical deformation of the fiber. The self-correlation analysis is performed for the same 36 × 16 × 16 = 9216 cells that are used in the calculation of the correlation coefficients shown in Fig. 7. Since the average values of the parameters, such as atomic stress σ_{xx}, atomic strain ε_{xx}, and density ρ, change with the level of deformation, we consider normalized values for each parameter. For example, we introduce normalized stress defined as $\sigma^*_{xx} = \frac{\sigma^{cell}_{xx} - \bar{\sigma}_{xx}}{SD(\sigma_{xx})}$, where σ^{cell}_{xx} is the average axial stress calculated for a given cell, $\bar{\sigma}_{xx}$ and $SD(\sigma_{xx})$ are the mean and standard deviation of the values calculated for all cells.

The changes in the normalized stress in each cell with increasing system strain are visualized in Fig. 11a–d. In each of these plots, the cells are ordered and assigned consecutive indexes in the order of increasing normalized stress at a reference strain ε_0. The normalized stress in each cell is then color coded from blue to red and is shown as a function of system strain in Fig. 11a–d. In the first three panels, Fig. 11a–c, the cells are ordered by the normalized stress at reference strains of 0.5%, 5.1%, and 10.4%, respectively, and the evolution of the stress in each cell is shown from ε_0 up to a system strain of 11.5%, just below the onset of fracture. If the elements of the CF nanostructure that are holding the stress at ε_0 would continue to do so upon further deformation (*i.e.*, in the absence of the nanoscale load redistribution), the initial color distribution from blue to red would be retained and the stress color map would look similar to that shown in Fig. 11g for the normalized local density. This is clearly not the case for the stress color maps, where the order of the normalized stress with cell index at the reference strains rapidly diminishes within about 0.5% increment of the system strain. After the initial drop in the correlation with the initial state, only a small level of "memory" for the initial color at ε_0 is still retained, as the system undergoes further tensile deformation. We also notice that the loss of the correlation with the initial stress/color is particularly pronounced for the small reference strain of $\varepsilon_0 = 0.5\%$, Fig. 11a, where the cells that have similar normalized stress (similar color) at the reference strain ε_0 exhibit an almost random distribution of normalized stress at higher strains. With an increased reference strain ε_0, however, the cells are more likely to keep their high or low normalized stress state during the deformation, as indicated by the extended red and blue areas in the top and bottom parts of the color maps shown in Fig. 11b and c. This observation suggests that the cells have a higher tendency to retain their stress levels at the later stage of the deformation.

Interestingly, ordering the cells by the final reference strain of $\varepsilon_0 = 11.5\%$, Fig. 11d, reveals a substantially stronger backward correlation between the stress states at ε_0 and the ones at preceding strain values as compared to the forward correlation with the initial stress state at $\varepsilon_0 = 0.5\%$ shown in Fig. 11a. The stronger backward correlation indicates that the elements of the nanostructure holding the stress just before the fracture are the ones that are more likely to support high stress at earlier stages of the deformation as well.

To further quantify the visual picture of the nanoscale load redistribution provided by Fig. 11a–d, we calculate the self-correlation coefficients for the normalized stress as a function of relative strain $\Delta\varepsilon$ with respect to the values of ε_0, $\frac{1}{N}\sum_{i=1}^{N}\sigma^*_{xx}(\varepsilon_0)\sigma^*_{xx}(\varepsilon_0 + \Delta\varepsilon)$, where $N = 9216$ is the number of cells used in the analysis. The results of the calculation are plotted in Fig. 11e for the same four values of ε_0 that are used in the color maps shown in Fig. 11a–d. As the strain increases by a small $\Delta\varepsilon$ from the initial level of ε_0, the self-correlation coefficients plotted by three solid lines in Fig. 1e plummet sharpy from the maximum value of 1 at $\Delta\varepsilon = 0\%$ to a level that depend on the value of ε_0. The larger is the reference strain ε_0, the higher is the level of self-correlation at larger strains. Moreover, the self-correlation coefficients exhibit a moderate increase with increasing $\Delta\varepsilon$ for ε_0 equal to 5.1% and 10.4%. Going backward by decreasing the strain from $\varepsilon_0 = 11.5\%$ (corresponds to the color map in Fig. 11d) reveals a rather different trend, where the self-correlation coefficient decreases gradually after an initial drop, as shown by the blue dashed line in Fig. 11e. The results of the self-correlation analysis

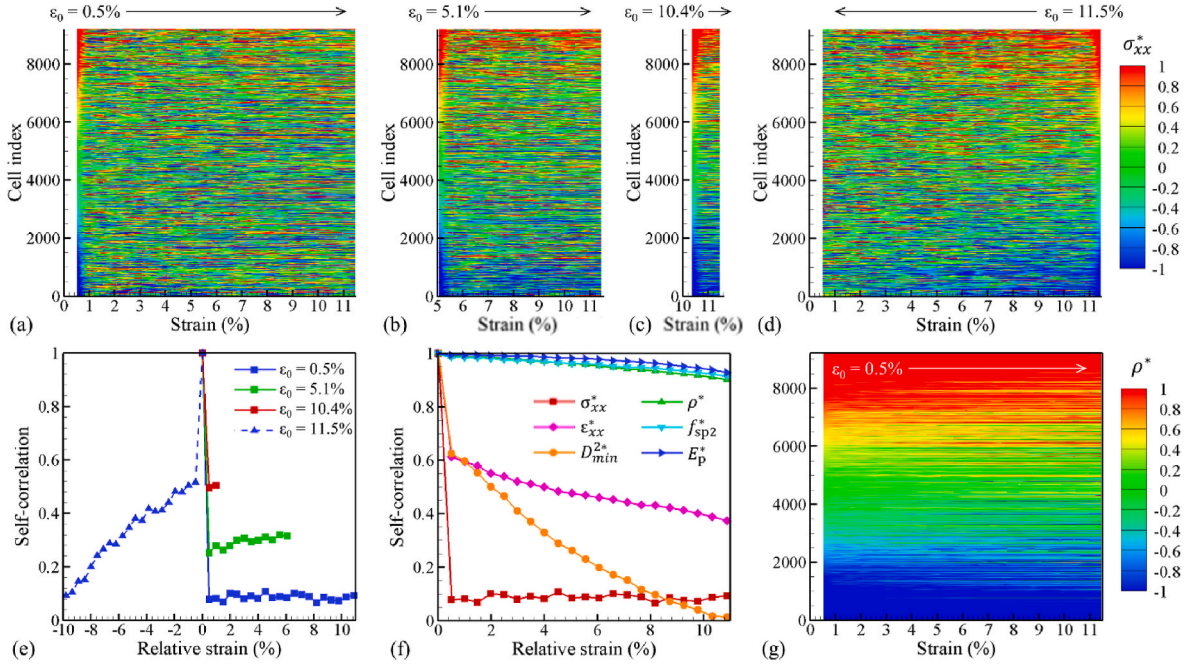

Fig. 11. Self-correlation analysis of the evolution of local structural and mechanical parameters in the computational sample CF2 during the tensile deformation: (a–d) Color maps showing the evolution of the normalized stress σ^*_{xx} calculated for each of the 36 × 16 × 16 = 9216 cells produced by spatial discretization of the system. The cells are ordered and indexed according to the increasing normalized stress at reference strains of $\varepsilon_0 = 0.5\%$ (a), $\varepsilon_0 = 5.1\%$ (b), $\varepsilon_0 = 10.4\%$ (c), and $\varepsilon_0 = 11.5\%$ (d). (e) Self-correlation coefficients calculated for the normalized stress and plotted as functions of relative strain, $\Delta\varepsilon = \varepsilon - \varepsilon_0$, for different values of the reference strain ε_0. (f) Self-correlation coefficients calculated for different parameters characterizing structure and mechanical deformation of the CF as a function of relative strain $\Delta\varepsilon$ with $\varepsilon_0 = 0.5\%$. (g) Color map of the evolution of normalized density ρ^* during the tensile deformation of the CF, with cells indexed and ordered so that the normalized density increases with the cell index at $\varepsilon_0 = 0.5\%$.

are consistent with the intuitive picture provided by the color maps of Fig. 11a–d and suggest a remarkable propensity of the CF for the nanoscale load redistribution, particularly at the early stage of the deformation process. With an increasing strain level, some of the stiff but initially loose structural elements may be fully stretched and start holding an increasingly high stress until the fracture. The self-correlation trends shown in Fig. 11e are defined by the fraction of such structural elements at the reference strain ε_0 and by the structural rearrangements activating and deactivating the load bearing structural elements during the subsequent deformation.

The connections between the nanoscale stress redistribution and the structural changes in the course of the tensile deformation can be explored by extending the self-correlation analysis to the normalized values of strain ε^*_{xx}, minimum square displacement difference D^{2*}_{min}, density ρ^*, fraction of sp^2 carbon f^*_{sp2}, and potential energy E^*_p. These local characteristics are calculated for each cell, and the corresponding self-correlation coefficients are plotted as functions of relative strain $\Delta\varepsilon$ with respect to the reference strain of $\varepsilon_0 = 0.5\%$ in Fig. 11f. The self-correlation coefficients for the local characteristics of mechanical deformation, ε^*_{xx} and D^{2*}_{min}, are decreasing with increasing system strain, although their decay is not as sharp as the one observed for the local stress. The gradual loss of self-correlation for ε^*_{xx} and D^{2*}_{min} suggests that the strain and non-affine deformation are not localized at the locations predefined by the initial structure but are continuously redistributed throughout the system during the deformation. In contrast to the sharp drop of the self-correlation coefficient for σ^*_{xx} and a more gradual but steady decay of the self-correlation observed for ε^*_{xx} and D^{2*}_{min}, the self-correlation coefficients calculated for the local structural characteristics, such as the normalized density, fraction of sp^2 carbon atoms, and potential energy, remain close to the initial levels throughout the deformation process. Since the number of cells is unchanged during the deformation of the system, each cell corresponds to roughly the same material regardless of the strain level. Thus, the preservation of the high levels of self-correlation is a clear indication that the structural rearrangements involved in the nanoscale stress redistribution do not involve significant changes in the local chemical bonding and density. To reinforce the connection between the plots of self-correlation coefficients and the color maps used in the analysis of the local stresses in Fig. 11a–d, we also provide a color map illustrating the evolution of the normalized density in each cell in Fig. 11g. The preservation of the local density suggested by the self-correlation plot in Fig. 11f is also clearly manifested in the color map in Fig. 11g.

Overall, the analysis of the nanoscale mechanisms of mechanical deformation and fracture of the computational CF structure suggests that the remarkable strength of the CF can be related to the ability of a nanostructure consisting of the curved and folded layers of turbostratic carbon to undergo continuous structural rearrangements up to the strain levels exceeding 11%. These structural rearrangements do not involve chemical bond scission but enable nanoscale stress redistribution during the deformation. The nanoscale uniformity of the computational samples is likely to be an important factor responsible for the much higher values of the tensile strength and fracture strain as compared to those observed in the experiments. Therefore, in the next section, we provide an additional analysis of the effect of nanovoids on the mechanical properties of the computational carbon fibers.

3.4. *Effect of nanovoids on stress concentration and mechanical properties*

The presence of voids and other stress-concentrating defects is considered to be one of the key factors limiting the tensile strength and fracture strain of the experimental CFs [3,12–17,29,30,43]. As discussed in Section 3.1, the nanovoids present in the computational samples have highly elongated shapes, tend to be aligned along the fiber axes, and can extend up to 20 nm in length. While the dimensions of the largest voids in the computational samples are comparable to those measured in the X-ray diffraction probing of PAN-based CFs [3,12,43,76], the tensile strength measured in experiments is defined by the largest voids present in the macroscopic samples and can be expected to increase logarithmically with the length of CF samples [86]. Moreover, the elongated axially-aligned nanovoids formed within the wrinkles and folds of graphene layers in the computational CFs may have a reduced ability for stress concentration as compared to the critical flaws generated in the CF manufacturing process. Indeed, although the computational sample CF1 features the longest nanovoid (Fig. 2) and has the lowest tensile strength out of the four computational samples, the difference in strength between the samples is relatively small, within 12%, and all samples exhibit strength that is substantially higher than the experimental values.

Thus, to provide additional insights into the effect of nanovoids on the tensile strength of CFs, we performed an additional simulation for a CF containing a nanovoid with a regular spherical shape. The system is generated by cutting a nanovoid with diameter of 6 nm in the computational sample CF2. The size of the nanovoid is similar to that of a critical crack estimated by extrapolating the results of loop test measurements to the strength of a disordered constituent of PAN-based CFs [17]. The computational sample with the spherical nanovoid is then subjected to the tensile testing performed with the same procedure as described in Section 2.4. Somewhat unexpectedly, the presence of the spherical void is found to have a relatively small effect on the mechanical response of the CF. The stress-strain curve is similar to that shown for the original sample CF2 in Fig. 4b and is characterized by a Young's modulus of 283 GPa, very close to the value of 287.4 GPa listed in Table 3 for the sample CF2. The presence of the spherical nanovoid does lead to a reduction of the tensile strength and fracture strain, although this reduction is rather moderate, from 34.6 GPa to 32.7 GPa for the strength and from 11.9% to 11.2% for the fracture strain.

The weak effect of the introduction of the spherical void on the mechanical properties of the computational sample can be explained by considering the evolution of the axial stress distribution, shown in the left panels of Fig. 12 for a 2-nm-thick slice cut from the center of the system along the *x*-*y* plane. As the strain increases, the shape of the nanovoid deforms into an ellipsoid elongated along the fiber axis, and the stress concentration in the vicinity of the nanovoid increases. Both the magnitude and the spatial extent of the stress generated by the nanovoid, however, remains comparable to the stress variations produced by the nanoscale stress redistribution discussed above, in Section 3.3.

To provide a "clean" view of the stress concentration around the void, without the interference from the natural stress variations in the CF nanostructure, we performed a continuum-level finite element method (FEM) modeling of the CF with a nanovoid using ANSYS software. The continuum model is parametrized to reproduce the mechanical properties of the computational sample CF2. The dimensions of the computational system and the nanovoid match those in the atomistic model. The stress distributions obtained in the continuum simulations are shown in the right panels of Fig. 12. The distributions match those expected from the theoretical analysis of the stress concentration on the surface of a void subjected to a uniaxial tensile stress [87]. The stress concentration factor, defined as the ratio of the maximum normal stress σ_{max} over the average normal stress in the whole system, is estimated to be around 1.7 in the FEM simulations, which quantitatively agrees with the theoretical value calculated in Ref. [87] for a similar void geometry.

The evolution of stress in the atomistic model of CF with an initially spherical nanovoid (left panels in Fig. 12) is thus produced by the combined effect of the stress concentration around the nanovoid (right panels in Fig. 12) and the natural nanoscale variations of stress within the CF nanostructure (Fig. 6). The ability of the CF nanostructure to adapt to the mechanical loading through the nanoscale stress redistribution, discussed in Section 3.3, is also helping to accommodate the stresses generated around the ellipsoidal void up to the values of σ_{max} exceeding 50 GPa. Eventually, the fracture is initiated at the location of

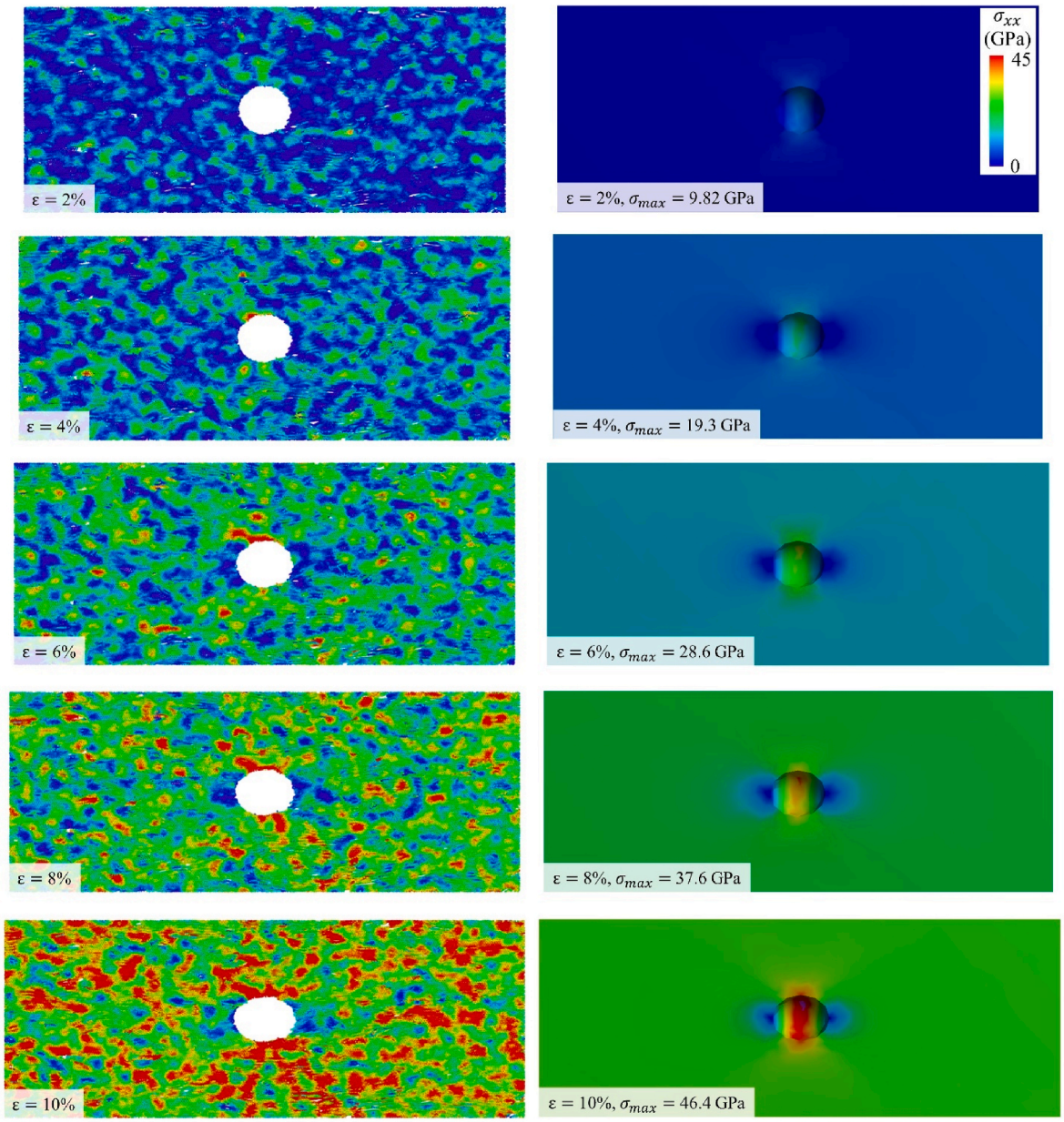

Fig. 12. Evolution of the stress distribution in a carbon fiber containing an initially spherical nanovoid with diameter of 6 nm predicted in MD (left panels) and FEM (right panels) simulations of tensile deformation. The values of strain are indicated on the panels. In the MD simulation, the void is introduced in the middle of sample CF2, and the stress distributions are shown for 2-nm-thick slices cut from the center of the system along a plane parallel to the axis of the fiber (*x*-*y* plane). The atoms are colored based on the atomic stress averaged over neighboring atoms located within a cutoff distance of 9 Å. The right panels show cross-sectional views of a half of the system used in the FEM modeling. The maximum values of the normal stress, σ_{max}, are marked on the panels. (A colour version of this figure can be viewed online.)

the stress concentration around the void, leading to the propagation of crack, as illustrated in the snapshots shown in Fig. 13. Note that the location of fracture is different in the simulations of CFs with and without the spherical void, and the two systems are shifted by different distances along the fiber axis to ensure that the locations where the fracture occurs are aligned with the centers of the snapshots.

The result of the simulation performed for the CF sample with a spherical void suggests that individual voids with sizes comparable to (a few times larger than) the characteristic size of the natural stress variations within the CF nanostructure are unlikely to be responsible for the reduction of the tensile strength and fracture strain down to the levels observed in the experiments. The larger internal voids, foreign inclusions, surface flaws, collective effect of multiple voids/defects, and/or stress concentration due to the presence of stiff graphitic crystallites can be the factors contributing to the deterioration of the mechanical properties with respect to the homogeneous nanostructure of the computational samples. Computational analysis of the effect of multiple voids and other mesoscale structural heterogeneities calls for an advanced multiscale modeling combining a continuum-level (extended FEM or peridynamics [88,89]) analysis of the stress distribution and failure with atomistic simulations of the critical elements of the microstructure.

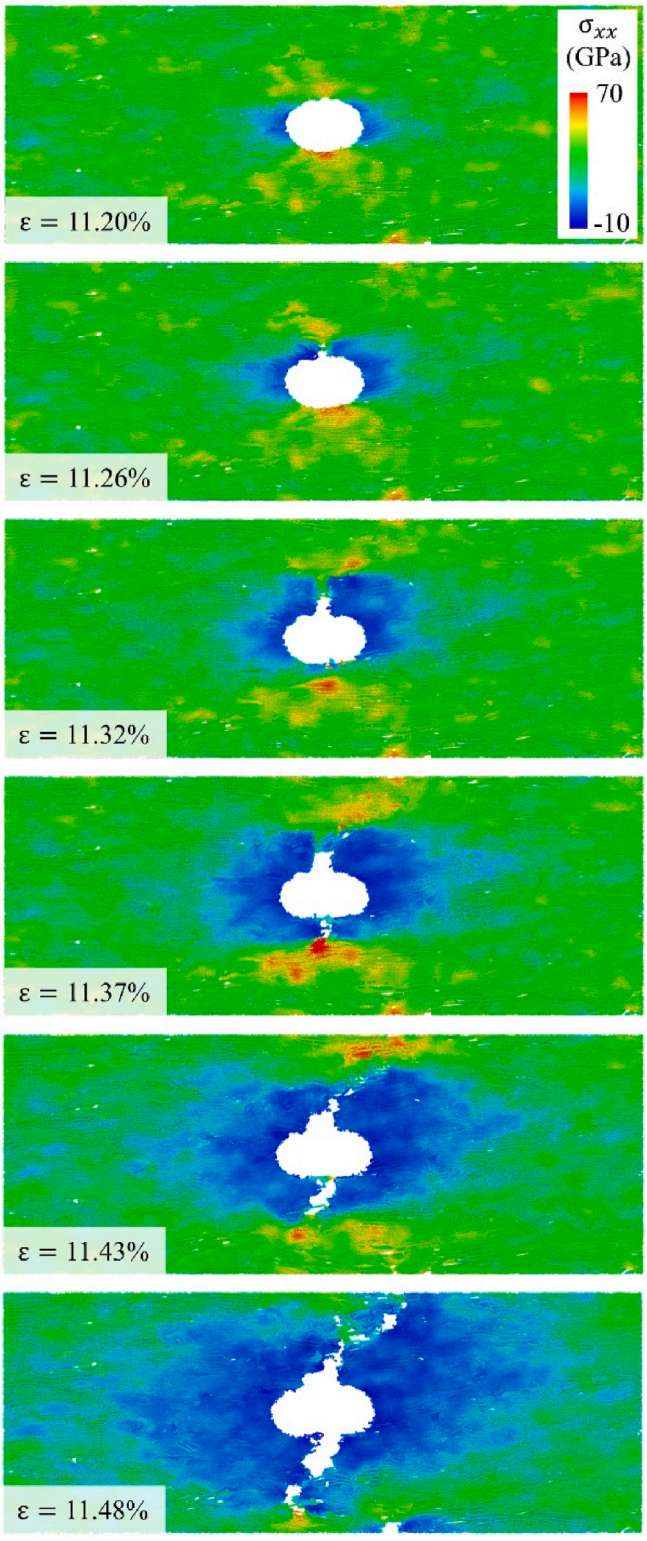

Fig. 13. Snapshots from the final stage of the MD simulation of the tensile deformation a CF containing an initially spherical nanovoid with diameter of 6 nm. The snapshots show 2-nm-thick slices cut from the center of the computational CF sample along a plane parallel to the axis of the fiber (*x*-*y* plane). The values of strain are indicated on the panels. The atoms are colored based on the atomic stress averaged over neighboring atoms located within a cutoff distance of 9 Å. (A colour version of this figure can be viewed online.)

4. Summary

The mechanisms of tensile deformation and fracture of carbon fibers are investigated in a series of large-scale MD simulations performed for four computational samples. The samples are generated through structural self-assembly and reactive fusion of idealized carbon ladder structures similar to those present in stabilized PAN fibers used in the CF manufacturing. All computational samples have homogeneous nanostructure featuring extensively curved and folded layers of turbostratic carbon, elongated nanovoids aligned along the fiber axes, and small isolated islands of ordered graphitic structure. The variation of parameters of the sample preparation procedure, such as the levels of compression and the dehydrogenation rate, enables the generation of CFs with different structural characteristics, such as relative fractions of turbostratic, graphitic, and amorphous constituents, as well as different pore size distributions. To facilitate comparison with experimental data, the diffraction profiles and 2D patterns are calculated and used for evaluation of sizes and shapes of the graphitic regions, as well as the degree of the structural alignment along the fiber axes. Overall, the structural parameters of the computational CF samples are comparable to those measured for commercial PAN-based CFs, except for the absence of large (tens of nm or larger) voids, foreign inclusions, and graphitic regions.

The mechanical properties of the computational samples are evaluated based on the stress-strain curves predicted in MD simulations of tensile testing of the CFs. The shapes of the stress-strain curves feature an extended stage of elastic deformation followed by a sharp drop of the stress characteristic of brittle failure. The values of Young's modulus obtained from the stress-strain curves are in a good agreement with those reported for typical PAN-based carbon fibers. The tensile strength and fracture strain, however, are found to significantly exceed the values measured in experiments. In particular, the tensile strength predicted in the MD simulations, ~30–35 GPa, is about three times higher than the record values of ~13 GPa reported for PAN-based CFs [16,17], and is almost an order of magnitude higher than the tensile strength of commercially available CFs. In fact, the strength predicted for the CF samples is comparable to that of polycrystalline graphene [85] and is about 30% of the theoretical maximum strength of carbon fibers, commonly considered to be around 100 GPa [3,12,15,90].

A detailed atomic-scale analysis of the mechanical deformation is performed to explain the surprising ability of the model CF nanostructure, largely consisting of curved and folded layers of turbostratic carbon, to support such a high level of stresses. The complex nanoscale structural organization of CFs is found to result in the nanoscale heterogeneity of stress distribution, with regions of high stress coexisting with those relaxed to almost zero stress even at the highest levels of strain approaching the fracture strain. The analysis of correlations between the local structural and mechanical characteristics during the deformation of CFs reveals that the nanoscale regions supporting higher levels of local stress tend to have higher density, enhanced fractions of sp^2 carbon and 6-member rings, as well as higher levels of graphitization. In order to hold the mechanical load during the deformation, the regions capable of supporting the high stresses should be connected into a continuous network percolating through the whole system. The formation of the high-stress percolation clusters is indeed observed in the CFs undergoing tensile deformation. The clusters, however, are not static but undergo continuous evolution during the deformation. With an increasing strain level, some of the stiff but initially loose elements of the nanostructure become fully stretched and start holding an increasingly high stress, while other regions are relaxed. It is this transient, fluid nature of the load-bearing percolation clusters that is responsible for the resilience of the computational CF samples to fracture. The continuous nanoscale redistribution of the mechanical load prevents the localization of high stresses at the early stage of the deformation and enables the CF nanostructure to adapt to the increasing load up to a fracture strain in excess of 10%. Eventually, the fracture is initiated in a region featuring a

coexistence of stiffer and more compliant elements of the nanostructure, leading to a catastrophic failure of the CF sample.

The results of a simulation performed for a CF containing a spherical nanovoid with diameter of 6 nm suggests that individual voids or other structural heterogeneities with sizes comparable to the characteristic size of the natural stress variations within the CF nanostructure do not produce a significant reduction in the tensile strength and fracture strain of the CF. The presence of larger internal voids, cracks, foreign inclusions, surface flaws, or clusters of nanovoids and defects, on the other hand, are likely to be responsible to the deterioration of the mechanical properties with respect to the uniform nanostructure of the computational samples. In addition to the structural defects, large graphitic crystallites, which are stiffer and stronger than surrounding disordered and more compliant structures, may act as sources of stress concentration and lead to the initiation of brittle failure at reduced strain levels. The growth of the graphitic crystallites, on the other hand, is usually associated with an increase in the Young's modulus [14,21], thus reflecting the common trade-off between the material stiffness, strength, and extensibility. The nanoscale stress redistribution mechanisms revealed in the present simulations can provide guidance for the design of CF microstructures optimized for applications that require high strength at high strain and high toughness.

Overall, the results of the atomistic simulations suggest that elimination of critical mesoscopic structural defects (*e.g.*, internal voids, foreign inclusions, and surface flaws) and prevention of the coarsening of structural constituents (*e.g.*, growth of graphitic regions during high-temperature stage of the CF manufacturing process) can yield a substantial increase in the strength and ductility of conventional carbon fibers. The high degree of structural uniformity appears to be a prerequisite for preventing stress localization and enabling the adaptive mechanical behavior through the nanoscale load redistribution revealed in the simulations. The computational predictions highlight the importance of the design of new CF manufacturing and post-processing methods focused on the elimination of internal and surface flaws, mesoscopic heterogeneities, and stress concentrators.

CRediT authorship contribution statement

Miao He: Methodology, Software, Data curation, Writing, Visualization, Investigation. **Mikhail I. Arefev:** Methodology, Software, Writing, Visualization, Investigation. **Kaushik Joshi:** Methodology, Software, Data curation, Investigation. **Leonid V. Zhigilei:** Conceptualization, Methodology, Writing, Investigation, Supervision.

Declaration of competing interest

The authors declare that they have no known competing financial interests or personal relationships that could have appeared to influence the work reported in this paper.

Acknowledgements

Financial support for this word was provided by the U.S. Department of Energy's Office of Energy Efficiency and Renewable Energy (EERE) under the Vehicle Technologies Office Award Number DE-EE0008195. Computational support is provided by the National Science Foundation through the Extreme Science and Engineering Discovery Environment (Project TGDMR110090).

References

[1] X. Huang, Fabrication and properties of carbon fibers, Materials 2 (2009) 2369–2403.
[2] D. Choi, H.-S. Kil, S. Lee, Fabrication of low-cost carbon fibers using economical precursors and advanced processing technologies, Carbon 142 (2019) 610–649.
[3] E.A. Morris, M.C. Weisenberger, M.G. Abdallah, F. Vautard, H. Grappe, S. Ozcan, F. L. Paulauskas, C. Eberle, D. Jackson, S.J. Mecham, A.K. Naskar, High performance carbon fibers from very high molecular weight polyacrylonitrile precursors, Carbon 101 (2016) 245–252.
[4] A. Jana, T. Zhu, Y. Wang, J.J. Adams, L.T. Kearney, A.K. Naskar, J.C. Grossman, N. Ferralis, Atoms to fibers: identifying novel processing methods in the synthesis of pitch-based carbon fibers, Sci. Adv. 8 (2022), eabn1905.
[5] K.R. Brown, T.M. Harrell, L. Skrzypczak, A. Scherschel, H.F. Wu, X. Li, Carbon fibers derived from commodity polymers: a review, Carbon 196 (2022) 422–439.
[6] H.G. Chae, Y.H. Choi, M.L. Minus, S. Kumar, Carbon nanotube reinforced small diameter polyacrylonitrile based carbon fiber, Compos. Sci. Technol. 69 (2009) 406–413.
[7] Z. Gao, J. Zhu, S. Rajabpour, K. Joshi, M. Kowalik, B. Croom, Y. Schwab, L. Zhang, C. Bumgardner, K.R. Brown, D. Burden, J.W. Klett, A.C.T. van Duin, L.V. Zhigilei, X. Li, Graphene reinforced carbon fibers, Sci. Adv. 6 (2020), eaaz4191.
[8] Y. Zhang, B. Zhu, X. Cai, X. Yuan, S. Zhao, J. Yu, K. Qiao, R. Qin, Rapid in situ polymerization of polyacrylonitrile/graphene oxide nanocomposites as precursors for high-strength carbon nanofibers, ACS Appl. Mater. Interfaces 13 (2021) 16846–16858.
[9] D.D. Edie, The effect of processing on the structure and properties of carbon fibers, Carbon 36 (1998) 345–362.
[10] S.M. Aldosari, M. Khan, S. Rahatekar, Manufacturing carbon fibres from pitch and polyethylene blend precursors: a review, J. Mater. Res. Technol. 9 (2020) 7786–7806.
[11] J. Zhu, Z. Gao, M. Kowalik, K. Joshi, C.M. Ashraf, M.I. Arefev, Y. Schwab, C. Bumgardner, K. Brown, D.E. Burden, L. Zhang, J.W. Klett, L.V. Zhigilei, A.C. T. van Duin, X. Li, Unveiling carbon ring structure formation mechanisms in polyacrylonitrile-derived carbon fibers, ACS Appl. Mater. Interfaces 11 (2019) 42288–42297.
[12] S. Ozcan, F. Vautard, A.K. Naskar, Designing the structure of carbon fibers for optimal mechanical properties, in: Polymer Precursor-Derived Carbon, American Chemical Society, 2014, pp. 215–232.
[13] B.A. Newcomb, Processing, structure, and properties of carbon fibers, Compos. Part A Appl. Sci. Manuf. 91 (2016) 262–282.
[14] E. Frank, L.M. Steudle, D. Ingildeev, J.M. Spörl, M.R. Buchmeiser, Carbon fibers: precursor systems, processing, structure, and properties, Angew. Chem. Int. Ed. 53 (2014) 5262–5298.
[15] D. Jang, M.E. Lee, J. Choi, S.Y. Cho, S. Lee, Strategies for the production of PAN-Based carbon fibers with high tensile strength, Carbon 186 (2022) 644–677.
[16] H.G. Chae, B.A. Newcomb, P.V. Gulgunje, Y. Liu, K.K. Gupta, M.G. Kamath, K. M. Lyons, S. Ghoshal, C. Pramanik, L. Giannuzzi, K. Şahin, I. Chasiotis, S. Kumar, High strength and high modulus carbon fibers, Carbon 93 (2015) 81–87.
[17] H. Okuda, R.J. Young, F. Tanaka, J. Watanabe, T. Okabe, Tensile failure phenomena in carbon fibres, Carbon 107 (2016) 474–481.
[18] M.G. Northolt, L.H. Veldhuizen, H. Jansen, Tensile deformation of carbon fiber and the relationship with the modulus for shear between the basal planes, Carbon 29 (1991) 1267–1279.
[19] M.J. Behr, B.G. Landes, B.E. Barton, M.T. Bernius, G.F. Billovits, E.J. Hukkanen, J. T. Patton, W. Wang, C. Wood, D.T. Keane, J.E. Rix, S.J. Weigand, Structure-property model for polyethylene-derived carbon fiber, Carbon 107 (2016) 525–535.
[20] B.V. Cunning, B. Wang, T.J. Shin, R.S. Ruoff, Structure-directing effect of single crystal graphene film on polymer carbonization and graphitization, Mater. Horiz. 6 (2019) 796–801.
[21] T. Matsumoto, Mesophase pitch and its carbon fibers, Pure Appl. Chem. 57 (1985) 1553–1562.
[22] A. Takaku, M. Shiona, X-ray measurements and the structure of polyacrylonitrile- and pitch-based carbon fibres, J. Mater. Sci. 25 (1990) 4873–4879.
[23] K. Joshi, M.I. Arefev, L.V. Zhigilei, Generation and characterization of carbon fiber microstructure in atomistic simulations, Carbon 152 (2019) 396–408.
[24] F. Liu, H. Wang, L. Xue, L. Fan, Z. Zhu, Effect of microstructure on the mechanical properties of PAN-based carbon fibers during high-temperature graphitization, J. Mater. Sci. 43 (2008) 4316–4322.
[25] T. Kobayashi, K. Sumiya, Y. Fukuba, M. Fujie, T. Takahagi, K. Tashiro, Structural heterogeneity and stress distribution in carbon fiber monofilament as revealed by synchrotron micro-beam X-ray scattering and micro-Raman spectral measurements, Carbon 49 (2011) 1646–1652.
[26] Y. Sha, W. Yang, S. Li, L. Yao, H. Li, L. Cheng, H. Yan, W. Cao, J. Tan, Laser induced graphitization of PAN-based carbon fibers, RCS Adv 8 (2018) 11543–11550.
[27] X. Liu, C. Zhu, J. Guo, Q. Liu, H. Dong, Y. Gu, R. Liu, N. Zhao, Z. Zhang, J. Xu, Nanoscale dynamic mechanical imaging of the skin-core difference: from PAN precursors to carbon fibers, Mater. Lett. 128 (2014) 417–420.
[28] M. He, K. Joshi, L.V. Zhigilei, Computational study of the effect of core–skin structure on the mechanical properties of carbon nanofibers, J. Mater. Sci. 56 (2021) 14598–14610.
[29] Z. Hua, Y.J. Zhong, D.F. Li, Pores in PAN-based carbon fiber and effects of pore defects on mechanical properties, Mater. Sci. Forum 546–549 (2007) 1665–1668.
[30] J. Lu, W. Li, H. Kang, L. Feng, J. Xu, R. Liu, Microstructure and properties of polyacrylonitrile based carbon fibers, Polym. Test. 81 (2020), 106267.
[31] J. Liu, Z. Yue, H. Fong, Continuous nanoscale carbon fibers with superior mechanical strength, Small 5 (2009) 536–542.
[32] S.N. Arshad, M. Naraghi, I. Chasiotis, Strong carbon nanofibers from electrospun polyacrylonitrile, Carbon 49 (2011) 1710–1719.
[33] J. Cai, M. Naraghi, Non-intertwined graphitic domains leads to super strong and tough continuous 1D nanostructures, Carbon 137 (2018) 242–251.
[34] C. Sauder, J. Lamon, Prediction of elastic properties of carbon fibers and CVI matrices, Carbon 43 (2005) 2044–2053.

[35] W.N. Reynolds, J.V. Sharp, Crystal shear limit to carbon fibre strength, Carbon 12 (1974) 103–110.
[36] B. Saha, A. Furmanchuk, Y. Dzenis, G.C. Schatz, Multi-step mechanism of carbonization in templated polyacrylonitrile derived fibers: ReaxFF model uncovers origins of graphite alignment, Carbon 94 (2015) 694–704.
[37] Y. Wei, J. Chen, H. Zhao, X. Zang, Pressure-strengthened carbon fibers from mesophase pitch carbonization processes, J. Phys. Chem. Lett. 13 (2022) 3283–3289.
[38] T. Senda, Y. Yamada, M. Morimoto, N. Nono, T. Sogabe, S. Kubo, S. Sato, Analyses of oxidation process for isotropic pitch-based carbon fibers using model compounds, Carbon 142 (2019) 311–326.
[39] M. Kowalik, C. Ashraf, B. Damirchi, D. Akbarian, S. Rajabpour, A.C.T. van Duin, Atomistic scale analysis of the carbonization process for C/H/O/N-based polymers with the ReaxFF reactive force field, J. Phys. Chem. B 123 (2019) 5357–5367.
[40] Q. Mao, S. Rajabpour, M. Kowalik, A.C.T. van Duin, Predicting cost-effective carbon fiber precursors: unraveling the functionalities of oxygen and nitrogen-containing groups during carbonization from ReaxFF simulations, Carbon 159 (2020) 25–36.
[41] C. Jian, J.J. Adams, J.C. Grossman, N. Ferralis, Carbon fiber synthesis from pitch: insights from ReaxFF based molecular dynamics simulations, Carbon 176 (2021) 569–579.
[42] S. Desai, C. Li, T. Shen, A. Strachan, Molecular modeling of the microstructure evolution during carbon fiber processing, J. Chem. Phys. 147 (2017), 224705.
[43] C. Zhu, X. Liu, X. Yu, N. Zhao, J. Liu, J. Xu, A small-angle X-ray scattering study and molecular dynamics simulation of microvoid evolution during the tensile deformation of carbon fibers, Carbon 50 (2012) 235–243.
[44] N. Gupta, V.I. Artyukhov, E.S. Penev, B.I. Yakobson, Carbonization with misfusion: fundamental limits of carbon-fiber strength revisited, Adv. Mater. 28 (2016) 10317–10322.
[45] E.S. Penev, V.I. Artyukhov, B.I. Yakobson, Basic structural units in carbon fibers: atomistic models and tensile behavior, Carbon 85 (2015) 72–78.
[46] A. Ito, S. Okamoto, Using molecular dynamics to assess mechanical properties of PAN-based carbon fibers comprising imperfect crystals with amorphous structures, Int. J. Mech. Aero. Indus. Mechatr. Manufac. Eng. 7 (2013) 1839–1845.
[47] L. Shi, M. Sessim, M.R. Tonks, S.R. Phillpot, Generation and characterization of an improved carbon fiber model by molecular dynamics, Carbon 173 (2021) 232–244.
[48] L. Martínez, R. Andrade, E.G. Birgin, J.M. Martínez, PACKMOL: a package for building initial configurations for molecular dynamics simulations, J. Comput. Chem. 30 (2009) 2157–2164.
[49] S. Kumar, D.P. Anderson, A.S. Crasto, Carbon fiber compressive strength and its dependence on structure and morphology, J. Mater. Sci. 28 (1993) 423–439.
[50] T.C. O'Connor, J. Andzelm, M.O. Robbins, AIREBO-M: a reactive model for hydrocarbons at extreme pressures, J. Chem. Phys. 142 (2015), 024903.
[51] S. Plimpton, Fast parallel algorithms for short-range molecular dynamics, J. Comput. Phys. 117 (1995) 1–19.
[52] K. Mylvaganam, L.C. Zhang, Important issues in a molecular dynamics simulation for characterizing the mechanical properties of carbon nanotubes, Carbon 42 (2004) 2025–2032.
[53] Z. Ni, H. Bu, M. Zou, H. Yi, K. Bi, Y. Chen, Anisotropic mechanical properties of graphene sheets from molecular dynamics, Physica B 405 (2010) 1301–1306.
[54] O.A. Shenderova, D.W. Brenner, A. Omeltchenko, X. Su, L.H. Yang, Atomistic modeling of the fracture of polycrystalline diamond, Phys. Rev. B 61 (2000) 3877–3888.
[55] T. Belytschko, S.P. Xiao, G.C. Schatz, R.S. Ruoff, Atomistic simulations of nanotube fracture, Phys. Rev. B 65 (2002), 235430.
[56] H. Zhao, K. Min, N.R. Aluru, Size and chirality dependent elastic properties of graphene nanoribbons under uniaxial tension, Nano Lett. 9 (2009) 3012–3015.
[57] Y.J. Sun, Y.H. Huang, F. Ma, D.Y. Ma, T.W. Hu, K.W. Xu, Molecular dynamics simulation on double-elastic deformation of zigzag graphene nanoribbons at low temperature, Mater. Sci. Eng. B 180 (2014) 1–6.
[58] S.J. Plimpton, A.P. Thompson, Computational aspects of many-body potentials, MRS Bull. 37 (2012) 513–521.
[59] A.C.T. van Duin, S. Dasgupta, F. Lorant, W.A. Goddard III, ReaxFF: a reactive force field for hydrocarbons, J. Phys. Chem. A 105 (2001) 9396–9409.
[60] T.P. Senftle, S. Hong, M.M. Islam, S.B. Kylasa, Y. Zheng, Y.K. Shin, C. Junkermeier, R. Engel-Herbert, M.J. Janik, H.M. Aktulga, T. Verstraelen, A. Grama, A.C.T. van Duin, The ReaxFF reactive force-field: development, applications and future directions, Nat. Comput. Mater. 2 (2016), 15011.
[61] S.G. Srinivasan, A.C.T. van Duin, P. Ganesh, Development of a ReaxFF potential for carbon condensed phases and its application to the thermal fragmentation of a large fullerene, J. Phys. Chem. A 119 (2015) 571–580.
[62] B.D. Jensen, K.E. Wise, G.M. Odegard, Simulation of the elastic and ultimate tensile properties of diamond, graphene, carbon nanotubes, and amorphous carbon using a revised ReaxFF parametrization, J. Phys. Chem. A 119 (2015) 9710–9721.
[63] P. Toth, Nanostructure quantification of turbostratic carbon by HRTEM image analysis: state of the art, biases, sensitivity and best practices, Carbon 178 (2021) 688–707.
[64] Z. Lin, L.V. Zhigilei, Time-resolved diffraction profiles and atomic dynamics in short-pulse laser-induced structural transformations: molecular dynamics study, Phys. Rev. B 73 (2006), 184113.
[65] M.A. Short, P.L. Walker Jr., Measurement of interlayer spacings and crystal sizes in turbostratic carbons, Carbon 1 (1963) 3–9.
[66] M.I. Arefev, M.V. Shugaev, L.V. Zhigilei, Kinetics of laser-induced melting of thin gold film: how slow can it get? Sci. Adv. 8 (2022), eabo2621.
[67] https://CompMat.org/carbon-structure-analysis/.
[68] https://CompMat.org/2D-diffraction/.
[69] B.D. Jensen, K.E. Wise, G.M. Odegard, The effect of time step, thermostat, and strain rate on ReaxFF simulations of mechanical failure in diamond, graphene, and carbon nanotube, J. Comput. Chem. 36 (2015) 1587–1596.
[70] A.P. Thompson, S.J. Plimpton, W. Mattson, General formulation of pressure and stress tensor for arbitrary many-body interaction potentials under periodic boundary conditions, J. Chem. Phys. 131 (2009), 154107.
[71] M.L. Falk, J.S. Langer, Dynamics of viscoplastic deformation in amorphous solids, Phys. Rev. E 57 (1998) 7192–7205.
[72] https://www.ovito.org/.
[73] F. Shimizu, S. Ogata, J. Li, Theory of shear banding in metallic glasses and molecular dynamics calculations, Mater. Trans. 48 (2007) 2923–2927.
[74] O.V. Yazyev, S.G. Louie, Topological defects in graphene: dislocations and grain boundaries, Phys. Rev. B 81 (2010), 195420.
[75] M.A. Rozhkov, A.L. Kolesnikova, I.S. Yasnikov, A.E. Romanov, Disclination ensembles in graphene, Low Temp. Phys. 44 (2018) 918–924.
[76] W. Ruland, Carbon fibers, Adv. Mater. 2 (1990) 528–536.
[77] M.A. Short, P.L. Walker, Measurement of interlayer spacings and crystal sizes in turbostratic carbons, Carbon 1 (1963) 3–9.
[78] M.S. Folomeshkin, Y.V. Pisarevsky, P.A. Prosekov, Y.A. Volkovsky, A.S. Kumskov, Y.V. Grigoriev, E.A. Ligacheva, A.V. Targonskii, A.E. Blagov, M.V. Kovalchuk, X-ray diffraction analysis and electron microscopy of the carbon fiber structure, Crystallogr. Rep. 64 (2019) 1–5.
[79] Z. Kurban, A. Lovell, D. Jenkins, S. Bennington, I. Loader, A. Schober, N. Skipper, Turbostratic graphite nanofibres from electrospun solutions of PAN in dimethylsulphoxide, Eur. Polym. J. 46 (2010) 1194–1202.
[80] N. Iwashita, M. Inagaki, Relations between structural parameters obtained by X-ray powder diffraction of various carbon materials, Carbon 31 (1993) 1107–1113.
[81] D.P. Anderson, Carbon Fiber Morphology, II: Expanded Wide-Angle X-Ray Diffraction Studies of Carbon Fibers, University of Dayton Research Institute, Dayton, OH, 1991.
[82] Y. Huang, R.J. Young, Effect of fibre microstructure upon the modulus of PAN- and pitch-based carbon fibres, Carbon 33 (1995) 97–107.
[83] A. Perret, W. Ruland, The microstructure of PAN-base carbon fibres, J. Appl. Crystallogr. 3 (1970) 525–532.
[84] T. Egami, K. Maeda, V. Vitek, Structural defects in amorphous solids: a computer simulation study, Philos. Mag. A 41 (1980) 883–901.
[85] T. Zhang, X. Li, H. Gao, Fracture of graphene: a review, Int. J. Fract. 196 (2015) 1–31.
[86] J. Fontana, P. Palffy-Muhoray, St. Petersburg paradox and failure probability, Phys. Rev. Lett. 124 (2020), 245501.
[87] T. Davis, D. Healy, A. Bubeck, R. Walker, Stress concentrations around voids in three dimensions: the roots of failure, J. Struct. Geol. 102 (2017) 193–207.
[88] N. Prakash, B. Deng, R.J. Stewart, C.M. Smith, J.T. Harris, Investigation of microscale fracture mechanisms in glass–ceramics using peridynamics simulations, J. Am. Ceram. Soc. 105 (2022) 4304–4320.
[89] F. Baber, J.-W. Kim, G. Sauti, R.A. Wincheski, B.D. Jensen, K.E. Wise, E.J. Siochi, I. Guven, Microstructural exploration of a carbon nanotube yarn reinforced composite using a peridynamic approach, J. Compos. Mater. 56 (2022) 861–876.
[90] S. Chand, Review Carbon fibers for composites, J. Mater. Sci. 35 (2000) 1303–1313.